

Summary

2	1	Introduction	3
3	2	Pixel detectors	5
4	2.1	Signal formation	5
5	2.2	CCDs	6
6	2.3	Hybrid pixels	6
7	2.4	CMOS MAPS and DMPAS	7
8	2.4.1	DMAPS: large and small fill factor	8
9	2.4.2	A modified sensor	9
10	2.5	Analog front end	9
11	2.5.1	Preamplifier	9
12	2.6	Readout logic	11
13	3	Use of pixel detectors	14
14	3.1	Tracking in HEP	14
15	3.1.1	Hybrid pixels at LHC and at SuperKEKB	15
16	3.1.2	First attempts to MAPS	16
17	3.2	Other applications	17
18	3.2.1	Applicability to FLASH radiotherapy	18
19	4	TJ-Monopix1	22
20	4.1	The sensor	23
21	4.2	Front end	25
22	4.2.1	ALPIDE-like	25
23	4.3	Readout logic	26
24	4.3.1	Dead time measurements	28
25	4.4	Injection	30
26	4.5	Measurements with radioactive sources	32
27	4.6	Calibration of the ToT signal	32
28	4.7	Fe vs bias	32
29	5	Arcadia-MD1	34
30	5.1	The sensor	34
31	5.2	Readout logic and data structure	34
32	5.2.1	Matrix division and data-packets	34
33	6	Threshold and noise characterization	38
34	6.1	Threshold and noise: figure of merit for pixel detectors	38
35	6.2	TJ-Monopix1 characterization	39
36	6.2.1	Threshold and noise dispersion	39
37	6.2.2	Absolute calibration of ToT	39
38	6.3	ARCADIA-MD1 characterization	39
39	7	Test beam measurements	40
40	7.1	Testbeam motivation	40
41	7.2	Apparatus description	40
42	7.3	Measurements	40

43	A Pixels detector: a brief overview	42
44	A.1 Radiation damages	42
45	Bibliography	44
46	Characterization of monolithic CMOS pixel sensors for charged particle detectors and for high	
47	intensity dosimetry	

⁴⁸ **Chapter 1**

⁴⁹ **Introduction**

⁵⁰ Pixel detectors, members of the semiconductor detector family, have significantly been used at the
⁵¹ accelerator experiments for energy and position measurement. Because of their dimension (today
⁵² $\sim 30 \mu\text{m}$ or even better) and their spatial resolution ($\sim 5\text{-}10 \mu\text{m}$), with the availability of technology
⁵³ in 1980s they proved to be perfectly suitable for vertex detector in the inner layer of the detector.

⁵⁴ Despite the monolithic pixels came up with CCDs, invented in 1969 and fastly used in cameras,
⁵⁵ their usage had to wait for microelectronics developement: in MAPS device the readout electronics
⁵⁶ is build on the pixel's area, then the pixel dimension is limited by the dimension of transistors. This
⁵⁷ constraint favoured the usage in physics experiment of hybrid pixels, which currently constitute
⁵⁸ the state-of-art for large scale pixel detector. These ones are made by two different wafer each one
⁵⁹ containing or the sensor or the ASIC, which are after joined together through microconnection.
⁶⁰ This structure allows a separate optimization for the two components and makes hybrid pixels
⁶¹ flexible and versatile.

⁶² Requirement imposed by accelerator are stringent and they will be even more with the increase
⁶³ of luminosity in terms of radiation hardness, efficiency and occupancy, time resolution, material
⁶⁴ budget and power consumption. For this reason experiments (as ATLAS, CMS, BelleII) began to
⁶⁵ look at the more innovative and well-performing monolithic active pixels (MAPS) as perspective for
⁶⁶ their future upgrades.

⁶⁷ Che condiziona la risoluzione e l'efficienza di ricostruzione della sua traccia, e consumi del
⁶⁸ detector, sono diventati sempre più rilevanti; molti esperimenti (ATLAS, CMS, BelleII,..) stanno
⁶⁹ infatti valutando la possibilità di sostituire gli ibridi con i MAPS, che per i temi precedenti offrono
⁷⁰ prestazioni migliori, a scapito di tempi di lettura mediamente più lunghi, vista anche la positiva
⁷¹ esperienza di ALICE ad LHC, primo esperimento ad introdurre un detector a pixel monolitico.

⁷² During my thesys I studied and characterised two monolithic active pixel chips, TJ-Monopix1
⁷³ and MD1; this devices, that are still prototypes, have been conceived and designed for physics
⁷⁴ experiments at colliders, space experiments and also for medical applications.

⁷⁵ il primo, TJ-Monopix1, è un prototipo di un modello selezionato per l'upgrade di Belle II
⁷⁶ durante il LSD nel 2025 (il chip finale si chiamerà OBELIX e avrà come sensore TJ-Monopix2,
⁷⁷ successore di Monopix1); il secondo chip è stato progettato da ARCADIA che potrà avere, nelle
⁷⁸ versioni future, applicazioni in fisica medica, in esperimenti nello spazio e ai collider.

⁷⁹ Le differenze principali tra i due chip risiedono nel segnale fornito in output (Monopix fornisce il
⁸⁰ tempo sopra soglia dell'impulso triangolare, proporzionale alla carica rilasciata nel sensore, mentre
⁸¹ arcadia fornisce un segnale puramente digitale), nella sequenza di readout dei pixel (monopix ha
⁸² una lettura puramente sequenziale di tipo "column drain") mentre arcadia ha una lettura più
⁸³ moderna che consente di poter aggregare dati durante la trasmissione (ad esempio nel caso di
⁸⁴ formazione di cluster e creazione di hti su pixel adiacenti).

⁸⁵ I performed a threshold and noise characterization ($\sim 400 \text{ e}^-$ and $\sim 15 \text{ e}^-$) of TJ-Monopix1 in
⁸⁶ order

⁸⁷ Tra i test con Monopix1 ho effettuato una caratterizzazione in soglia ($\sim 400 \text{ e}^-$) e rumore (\sim
⁸⁸ 15 e^-) al fine di visualizzare la dispersione di questi valori sulla matrice; per poter minimizzare la
⁸⁹ dispersione sulla matrice e avere una più uniforme selezione della soglia (che è globale su tutta
⁹⁰ la matrice), le versioni successive di TJ-Monopix1 includono e includeranno la possibilità di fare
⁹¹ piccole correzioni (3 bit per pixel vengono allocati in Monopix2) di quest'ultima pixel per pixel.
⁹² Per poter fornire le misure dei segnale fornito, tempo sopra soglia ToT, in elettroni, che assieme

93 alle lacune vengono create dal passaggio della particella incidente e che quindi sono la quantità
94 fisica "importante" nella misura, è stata necessaria una calibrazione assoluta dell'oggetto. Per
95 quest'ultima e per altri test ?? mi sono servita di sorgenti radiattive come il ferro 55 (emissione di
96 un fotone gamma a 5.9 kev e dello stronzio 90 il cui spettro dell'elettrone emesso ha un end point
97 a x) e dei cosmici. Inoltre ho partecipato ai test di Monopix1 su fascio: abbiamo testato il chip in
98 una modalità diversa da quella per cui è stato progettato (tracking) e più simile al funzionamento
99 delle CCD, in cui non si cerca di distinguere il singolo elettrone incidente ma si integra in un
100 singolo segnale di output la carica rilasciata da più elettroni incidenti. Il fascio utilizzato (elettroni
101 da 7-9 MeV) è un fascio ad altissima intensità e verrà utilizzato per fare ricerca su radioterapia
102 ad alto rate (l'acceleratore è in grado di rilasciare dosi -con riferimento in acqua- fino a 40 Gy/s,
103 corrispondenti ad un numero di particelle di ..). Per quanto riguarda, invece, le misure sul chip
104 MD1, ho partecipato ai test elettrici e sul front end di un prototipo non ancora completamente
105 funzionante. Un nuovo chip dovrebbe arrivare nei prossimi giorni a Pisa.

¹⁰⁶ **Chapter 2**

¹⁰⁷ **Pixel detectors**

¹⁰⁸ I pixel detector fanno parte della famiglia dei detector a semiconduttore e il loro funzionamento si
¹⁰⁹ basa sulla creazione di coppie elettrone lacuna all'interno del bulk. Dalla creazione della particella
¹¹⁰ incidente di queste coppie e facendole driftare attraverso l'applicazione di un campo elettrico, si
¹¹¹ ottiene quindi un segnale all'interno del rivelatore correlabile all'energia della particella incidente.
¹¹² Il campo elettrico applicato, lo spessore della zona di svuotamento, le modalità con cui il
¹¹³ segnale viene processato e trasmesso all'esterno del rivelatore sono caratteristiche specifiche del
¹¹⁴ tipo di chip. In questo capitolo tratterò dunque i principali tipi di rivelatori a pixel, sofferandomi
¹¹⁵ in particolare sui pixel monoliti.

¹¹⁶ **2.1 Signal formation**

¹¹⁷ When a charge particle passes through a pixel and loses energy by ionization a part of that
¹¹⁸ energy is used to generate electron-hole pairs (another part is used for other processes, as the
¹¹⁹ lattice excitation) which are then separated by the electric field and collected at their respectively
¹²⁰ electrodes (*p* for holes and *n* for electrons)¹; by the drift of these charges, a signal i_e is generated
¹²¹ on the electrode *e* as stated by the Shockley-Ramo's theorem:

$$i_e(t) = -q v(t) E_{WF,e} \quad (2.1)$$

¹²² where $v(t)$ is the instantaneous velocity of the charge q and E_{WF} is the weighting field, that is the
¹²³ field obtained biasing the electrode *e* with 1V and all the others with 0V. The drift velocity of the
¹²⁴ charge depends on the electric field and on the mobility of the particle:

$$v = \mu(E) E \quad (2.2)$$

¹²⁵ where $\mu(E)$ is a function of the electric field and is linear with E only for small E : at higher values
¹²⁶ the probability of interactions with optical phonons increases and the mobility drops and this leads
¹²⁷ to an independence of the velocity from the electric field (fig. 2.1b).

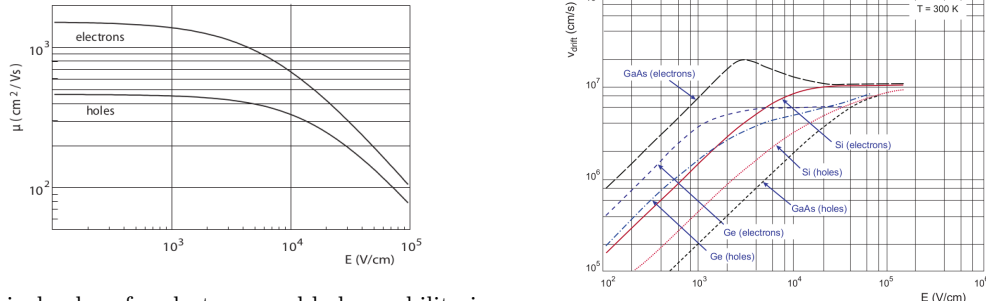
¹²⁸ The average energy needed to create a pair at 300 K in silicon is $w_i = 3.65$ eV, that is more
¹²⁹ than the mean ionization energy because of the interactions with phonon, since for a minimum
¹³⁰ ionizing particle (MIP) the most probable value (MPV) of charge released in the semiconductor is
¹³¹ 0.28 keV/ μ m, hence the number of electrons-vacuum pairs is:

$$\langle \frac{dE}{dx} \rangle \frac{1}{w_i} \sim 80 \text{ e}/\text{h} \sim \frac{1.28 \cdot 10^{-2} fC}{\mu m} \quad (2.3)$$

¹³² CON UN'INCERTEZZA CHE È RADICE DI N; ED EVENTUALEMTE SI AGGIUNGE IL
¹³³ FATTORE DI FANO NEL CASO DI ASSORBIMENTO TOTALE. IL FATTORE DI FANO È
¹³⁴ 0.115 NEL SILICIO. ecc

¹³⁵ It is fundamental that pairs e/h are produced in the depleted region of the semiconductor where
¹³⁶ the probability of recombination with charge carriers is low to avoid loss of signals. Pixel detectors

¹Even if in principle both the electrode can be used to read a signal, for pixel detectors, where the number of channel and the complexity of readout are high, only one is actually used. In strip and pad detectors, instead, is more common a dual-side readout



(a) Typical values for electrons and holes mobility in silicon at room temperature are $\mu_n \sim 1450 \text{ cm}^2/\text{Vs}$, $\mu_h = 500 \text{ cm}^2/\text{Vs}$
(b) Drift velocity at room temperature in different semiconductors

137 are then commonly reverse biased: a positive bias is given to the n electrode and a negative to the
138 p to grow the depletion zone in the epitaxial layer below the electrode. The width of the depletion
139 region is related with the external bias V_{ext} , the resistivity ρ and also with the dopant:

$$140 \quad d_n \sim 0.55 \sqrt{\frac{\rho}{\Omega cm}} \frac{V_{ext}}{V} \mu m \quad (2.4) \quad 141 \quad d_p \sim 0.32 \sqrt{\frac{\rho}{\Omega cm}} \frac{V_{ext}}{V} \mu m \quad (2.5)$$

143 For that reason high resistivity wafers ($100 \Omega cm - k\Omega cm$) are typically preferred because they
144 allow bigger depletion zone with smaller voltage bias. **Metto il disegno "standard" di una giunzione**

145 2.2 CCDs

146 **descrivi come sono fatte e come funziona il readout** Tens of ms due to the need to transfer the
147 charge signals pixel by pixel through a single output circuit For photon imaging the need of high
148 assorbtion efficiency, **per cui usi materiali con alto Z**

149 2.3 Hybrid pixels

150 **METTI IN EVIDENZAZ CHE PUOI FARE UN READOUT CON TECNOLOGIA CMOS.** Metti
151 **in evidenza che sono più veloci** Hybrid pixels are made of two parts (fig. 2.2a), the sensor and the
152 electronics: for each pixel these two parts are welded together through microconnection (bump
153 bond).

154 They provide a practical system where readout and sensor can be optimized separately, although
155 the testing is less easy-to-do since the sensor and the R/O must be connected together before.

156 In addition, the particular and sophisticated procedure to bond sensor and ASIC (application spe-
157 cific integrated circuit) makes them difficult to produce, delicate, especially when exposed to high
158 levels of radiation, and also expensive.

159 A critical parameter for accelerator experiments is the material budget, which represents the main
160 limit factor for momentum measurement resolution in a magnetic field; since hybrid pixels are
161 thicker (\sim hundreds of μm) than monolithic ones (even less than $100 \mu m$), using the latter the
162 material budget can be down by a third: typical value for hybrid pixels is $1.5 \% X_0$ per layer,
163 while for monolithic $0.5 \% X_0$.

164 Among other disadvantages of hybrid pixels there is the bigger power consumption that implies,
165 by the way, a bigger cooling system leading in turn to an increase in material too.

166 **DEPFET** are the first attempt towards the integration of the front end (FE) on the sensor bulk:
167 they are typically mounted on a hybrid structure but they also integrate the first amplification
168 stage.

169 Each pixel implements a MOSFET (metal-oxide-semiconductor field-effect transistor) transistor
170 (a p-channel in fig. 2.2b): an hole current flows from source to drain which is controlled by the
171 external gate and the internal gate together. The internal gate is made by a deep $n+$ implant

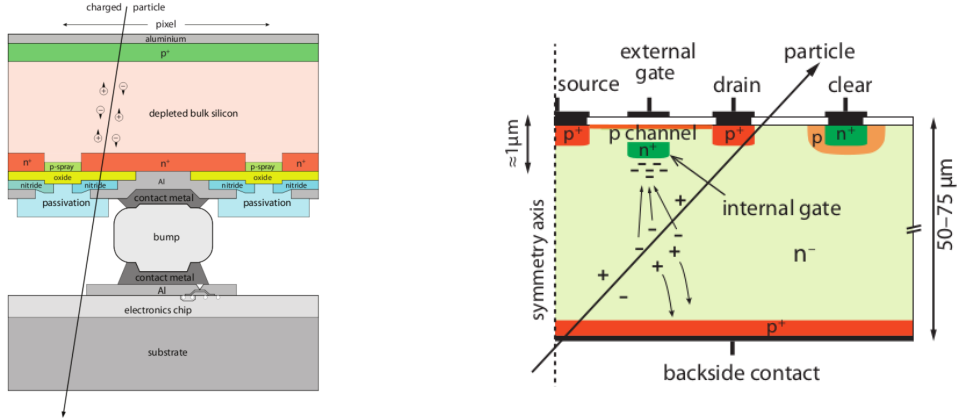


Figure 2.2: Concept cross-section of hybrid pixel (a) and of a DEPFET (b)

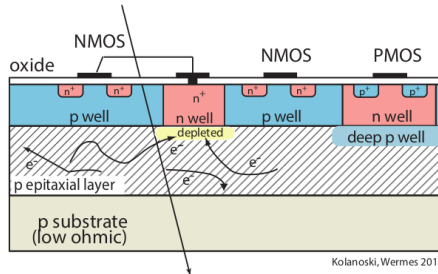


Figure 2.3: Concept cross-section of CMOS MPAS pixel

towards which electrons drift after being created in the depletion region (to know how the signal is created in a pixel detector look at appendix A); the accumulation of electrons in the region underneath the n implant changes the gate potential and controls the transistor current.
DEPFET typically have a good S/N ratio: this is principally due the amplification on-pixel and the large depletion region. But, since they need to be connected with ASIC the limiting factor still is the material budget.

2.4 CMOS MAPS and DMPAS

With respect to CCDs, the radiation tolerance could be greatly increased by sensing the signal charge within its own pixel, instead of transporting it over thousands of pixels. The readout speed could also be dramatically increased by in-pixel amplitude discrimination, followed by sparse readout of only the hit pixels. Monolithic active pixels accommodate on the same wafer both the sensor and the front end electronics, with the second one implanted on top within a depth of about 1 μm below the surface.

MAPS have been first proposed and realized in the 1990s and their usage has been enabled by the development of the electronic sector which guarantees the decrease in CMOS transistors dimension at least every two years, as stated by the Moore's law².

As a matter of fact the dimension of components, their organization on the pixel area and logic density are important issues for the design and for the layout; typically different decisions are taken for different purposes.

Monolithic active pixel can be distinguished between two main categories: MAPS and depleted MAPS (DMPAS).

MAPS (figure 2.3) have typically an epitaxial layer in range 1 μm to 20 μm and because they are not depleted, the charge is mainly collected by diffusion rather than by drift. This makes the path of charges created in the bulk longer than usual, therefore they are slow (of order of 100 ns) and the collection could be partial especially after the irradiation of the detector (look at A for radiation damages), when the trapping probability become higher.

²Moore's law states that logic density doubles every two years.

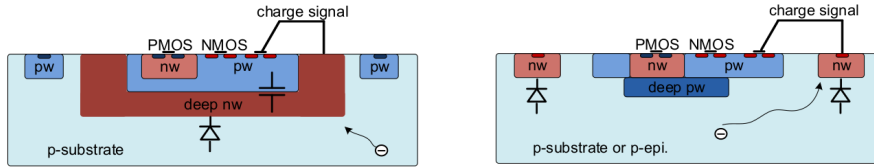


Figure 2.4: Concept cross-section with large and small fill factor

199 In figure 2.3 is shown as example of CMOS MAPS: the sensor in the scheme implements an n well
 200 as collection diode; to avoid the others n wells (which contain PMOS transistor) of the electronic
 201 circuit would compete in charge collection and to shield the CMOS circuit from the substrate,
 202 additionally underlying deep p well are needed. DMAPS are instead MAPS depleted with d
 203 typically in $\sim 25 \mu\text{m}$ to $150 \mu\text{m}$ (eq. 2.1) which extends from the diode to the deep p-well, and
 204 sometimes also to the backside (in this case if one wants to collect the signal also on this electrode,
 205 additional process must be done).

206 2.4.1 DMAPS: large and small fill factor

207 There are two different sensor-design approaches (figure 2.4) to DMAPS:

- 208 • large fill factor: a large collection electrode that is a large deep n-well and that host the
 209 embedded electronics
- 210 • small fill factor: a small n-well is used as charge collection node

211 To implement a uniform and stronger electric field, DMAPS often uses large electrode design that
 212 requires multiple wells (typically four including deep n and p wells); this layout adds on to the
 213 standard terms of the total capacity of the sensor a new term (fig. 2.5), that contributes to the
 214 total amplifier input capacity. In addition to the capacity between pixels (C_{pp}) and between the
 215 pixel and the backside (C_b), a non-negligible contribution comes from the capacities between wells
 216 (C_{WW} and C_{SW}) needed to shield the embedded electronics. These capacities affect the thermal
 217 and 1/f noise of the charge amplifier and the τ_{CSA} too:

$$218 \quad ENC_{thermal}^2 \propto \frac{4}{3} \frac{kT}{g_m} \frac{C_D^2}{\tau_{sh}} \quad (2.6) \quad \tau_{CSA} \propto \frac{1}{g_m} \frac{C_D}{C_f} \quad (2.7)$$

219 where g_m is the transconductance, τ_{sh} is the shaping time.
 220 Among the disadvantages coming from this large input capacity could be the coupling between
 221 the sensor and the electronics resulting in cross talk: noise induced by a signal on neighbouring
 222 electrodes; indeed, since digital switching in the FE electronics do a lot of oscillations, this prob-
 lem is especially connected with the intra wells capacities. So, larger charge collection electrode

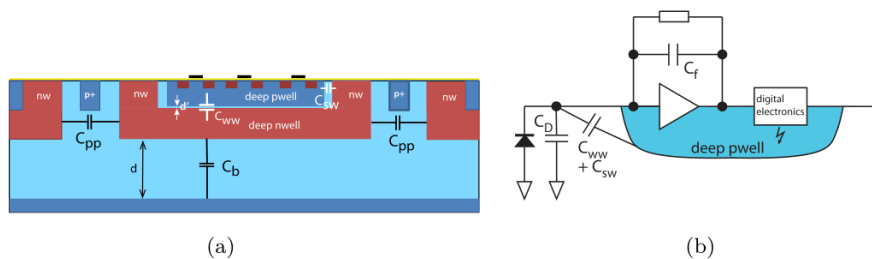


Figure 2.5: C_{pp} , C_b , C_{WW} , C_{SW}

223 sensors provide a uniform electric field in the bulk that results in short drift path and so in good
 224 collection properties, especially after irradiation, when trapping probability can become an issue.
 225 The drawback of a large fill-factor is the large capacity ($\sim 100 \text{ fF}$): this contributes to the noise
 226 and to a speed penalty and to a larger possibility of cross talk.

	small fill factor	large fill factor
small sensor C	✓ (< 5 fF)	✗ (~ 100 200 fF)
low noise	✓	✗
low cross talk	✓	✗
velocity performances	✓	✗ (~100 ns)
short drift paths	✗	✓
radiation hard	✗	✓

Table 2.1: Small and large fill factor DMAPS characteristics

228 The small fill-factor variant, instead, benefits from a small capacity (5 fF to 20 fF), but suffers
 229 from a not uniform electric field and from all the issue related to that. **Ho già detto prima parlando
 230 dei MAPS, devo ripetere qui?**

231 As we'll see these two different types of sensor require different amplifier: the large electrode one is
 232 coupled with the charge sensitive amplifier, while the small one with voltage amplifier (sec 2.5.1).

233 2.4.2 A modified sensor

234 A process modification developed by CERN in collaboration with the foundries has become the
 235 standard solution to combine the characteristics of a small fill factor sensor (small input amplifier
 236 capacity) and of large fill factor sensor (uniform electric field) is the one carried out for ALICE
 237 upgrade about ten years [1].

238 A compromise between the two sensors could also be making smaller pixels, but this solution
 239 requires reducing the electronic circuit area, so a completely new pixel layout should be though.
 240 The modification consists in inserting a low dose implant under the electrode and one its advantage
 241 lies in its versatility: both standard and modified sensor are often produced for testing in fact.

242 Before the process modification the depletion region extends below the diode towards the sub-
 243 strate, and it doesn't extend laterally so much even if a high bias is applied to the sensor (fig. 2.6).
 244 After, two distinct pn junctions are built: one between the deep p well and the n^- layer, and the
 245 other between the n^- and the p^- epitaxial layer, extending to the all area of the sensor.

246 Since deep p well and the p-substrate are separated by the depletion region, the two p electrodes
 247 can be biased separately³ and this is beneficial to enhance the vertical electric field component.
 248 The doping concentration is a trimmer parameter: it must be high enough to be greater than the
 249 epitaxial layer to prevent the punchthrough between p-well and the substrate, but it must also be
 250 lower enough to allow the depletion without reaching too high bias.

251 2.5 Analog front end

252 After the creation of a signal on the electrode, the signal enters the front end circuit (fig.2.7), ready
 253 to be molded and transmitted out of chip. Low noise amplification, fast hit discrimination and an
 254 efficient, high-speed readout architecture, consuming as low power as possible must be provided
 255 by the readout integrated electronics (ROIC).

256 Let's take a look to the main steps of the analog front end chain: the preamplifier (that actually
 257 often is the only amplification stage) with a reset to the baseline mechanism and a leakage current
 258 compensation, a shaper (a band-pass filter) and finally a discriminator. The whole chain must be
 259 optimized and tuned to improve the S/N ratio: it is very important both not to have a large noise
 260 before the amplification stage in order to not multiply that noise, and chose a reasonable threshold
 261 of the discriminator to cut noise-hits much as possible.

262 2.5.1 Preamplifier

263 Even if circuits on the silicon crystal are only constructed by CMOS, a preamplifier can be modeled
 264 as an operational amplifier (OpAmp) where the gain is determined by the input and feedback

³This is true in general, but it can be denied if other doping characteristics are implemented, and we'll see that this is the case of TJ-Monopix1

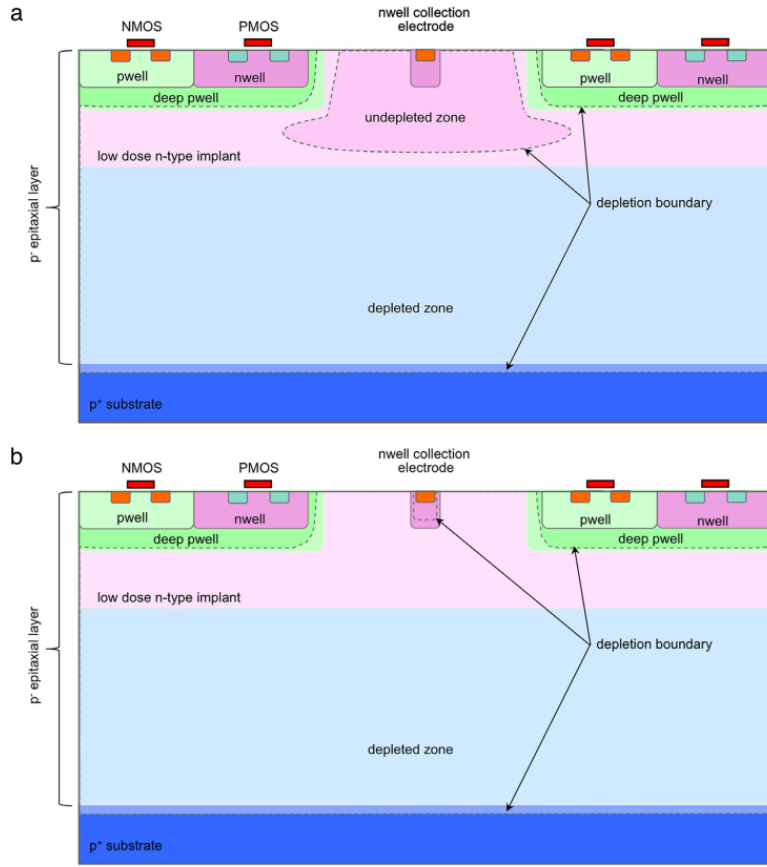


Figure 2.6: A modified process for ALICE tracker detector: a low dose n implant is used to create a planar junction. In (a) the depletion is partial, while in (b) the pixel is fully depleted.

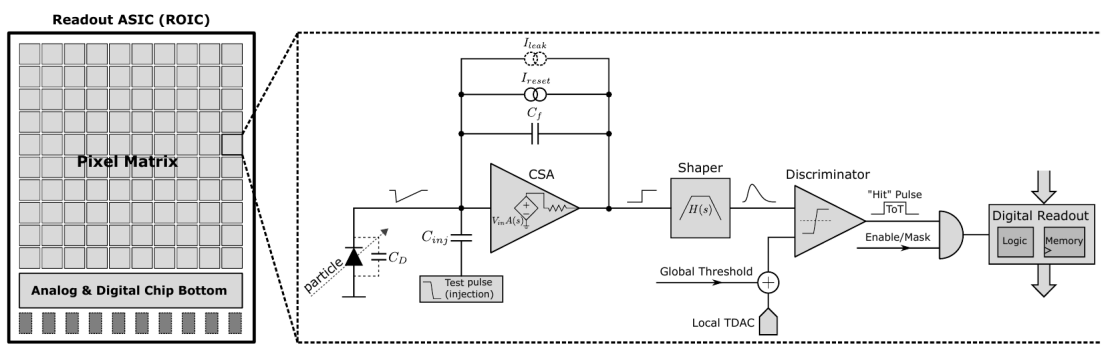


Figure 2.7: Readout FE scheme: in this example the preamplifier is a charge sensitive one (CSA) but changing the capacitive feedback into a resistive one, this can be converted in a voltage or current amplifier.

265 impedance (first step in figure 2.7):

$$G = \frac{v_{out}}{v_{in}} = \frac{Z_f}{Z_{in}} \quad (2.8)$$

266 Depending on whether a capacity or a resistance is used as feedback, respectively a charge or a
 267 voltage amplifier is used: if the voltage input signal is large enough and have a sharp rise time, the
 268 voltage sensitive preamplifier is preferred. Consequently, this flavor doesn't suit to large fill factor
 269 MAPS whose signal is already enough high: $v_{in} = Q/C_D \approx 3\text{fC}/100\text{ pF} = 0.03\text{ mV}$, but it's fine
 270 for the small fill factor ones: $v_{in} = Q/C_D \approx 3\text{fC}/3\text{ pF} = 1\text{ mV}$.

271 In the case of a resistor feedback, if the signal duration time is longer than the discharge time
 272 ($\tau = R_S C_D$) of the detector the system works as current amplifier, as the signal is immediately
 273 trasmit to the amplifier; in the complementary case (signal duration longer than the discharge
 274 time) the system integrates the current on the C_D and operates as a voltage amplifier.

275 2.6 Readout logic

276 Readout logic includes the part of the circuit which takes the FE output signal, processes it and
 277 then transmit it out of pixel and/or out of chip; depending on the situation of usage different
 278 readout characteristics must be provided.

279 To store the analogical information (i.e. charge collected, evolution of signal in time, ...) big buffers
 280 and a large bandwidth are needed; the problem that doesn't occur, or better occur only with really
 281 high rate, if one wants record only digital data (if one pixel is hit 1 is recorded, and if not 0 is
 282 recorded).

283 A common compromise often made is to save the time over threshold (ToT) of the pulse in clock
 284 cycle counts; this needs of relatively coarse requirement as ToT could be trimmer to be a dozen
 285 bits but, being correlated and hopefully being linear with the deposited charge by the impinging
 286 particle in the detector, it provides a sufficient information. The ToT digitalization usually takes
 287 advantage of the distribution of a clock (namely BCID, bunch crossing identification) on the pixels'
 288 matrix. The required timing precision is at least around 25 ns, that corresponds to the period of
 289 bunch collisions at LHC; for such reason a reasonable BCID-clock frequency for pixels detector is
 290 40 MHz.

291 Leading and trailing edges' timestamp of the pulse are saved on pixel within a RAM until they
 292 have been read, and then the ToT is obtained from their difference.

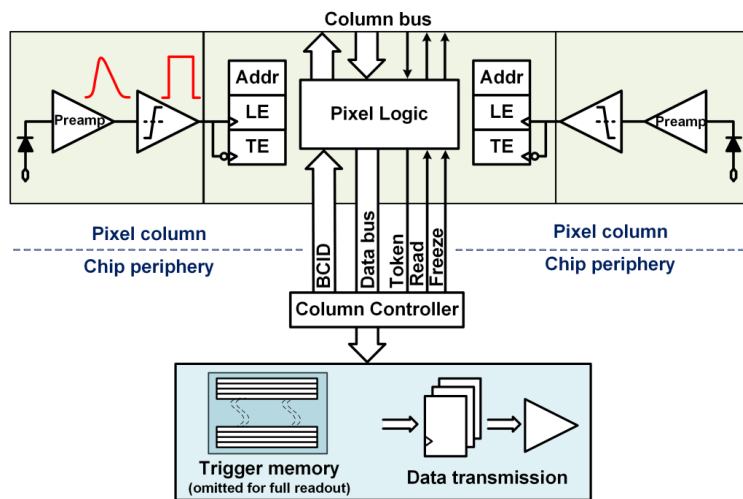


Figure 2.8: Column drain R/O scheme where ToT is saved

292 Moreover, the readout architecture can be full, if every hit is read, or triggered, if a trigger
 293 system decides if the hit must be store or not. On one hand the triggered-readout needs buffers
 294 and storage memories, on the other the full readout, because there is no need to store hit data on
 295 chip, needs an high enough bandwidth.

296 A triggered readout is fundamental in accelerator experiments where the quantity of data to store
 297 is too large to be handled, and some selections have to be applied by the trigger: to give an order

299 of growth, at LHC more than 100 TBit/s of data are produced, but the storage limit is about 100
300 MBit/s [2] (pag. 797).

301 Typically the trigger signal is processed in a few μs , so the pixel gets it only after a hundred clock
302 cycles from the hit arrival time: the buffer depth must then handle the higher trigger latency.

303 After having taken out the data from the pixel, it has to be transmitted to the end of column
304 (EoC) where a serializer deliver it out of chip, typically to an FPGA.

305 There are several ways of transmitting data from pixel to the end of column: one of the most
306 famous is the column-drain read out, developed for CMS and ATLAS experiments [3]. All the
307 pixels in a double-column share a data bus and only one pixel at a time, according to a priority
308 chain, can be read. The reading order circuit is implemented by shift register (SR): when a hit
309 arrives, the corresponding data, which can be made of timestamp and ToT, is temporarily stored
310 on a RAM until the SH does not allow the access to memory by data bus.

311 Even if many readout architectures are based the column-drain one, it doesn't suit for large size
312 matrices. The problem is that increasing the pixels on a column would also raise the number of
313 pixels in the priority chain and that would result in a slowdown of the readout.

314 If there isn't any storage memory, the double-column behaves as a single server queue and the
315 probability for a pixel of waiting a time T greater than t , with an input hit rate on the column μ
316 and an output bandwidth B_W is [4]:

$$P(T > t) = \frac{\mu}{B_W} e^{-(B_W - \mu)t} \quad (2.9)$$

317 To avoid hit loss (let's neglect the contribution to the inefficiency of the dead time τ due to the
318 AFE), for example imposing $P_T > t \sim 0.001$, one obtains $(B_W - \mu) t_t \sim 6$, where t_t is the time
319 needed to transfer the hit; since t_t is small, one must have $B_W \gg \mu$, that means a high bandwidth
[4].

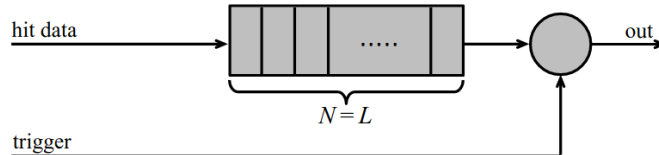


Figure 2.9: Block diagram of a pipeline buffer: N is the dimension of memory buffer and L is the trigger latency expressed in BCID cycles

320 Actually the previous one is an approximation since each pixel sees a different bandwidth de-
321 pending on the position on the queue: the first one sees a full bandwidth, but the next sees a
322 smaller one because occasionally it can be blocked by the previous pixel. Then the bandwidth seen
323 by the pixel i is $B_i = B - \sum_j \mu_j$, where μ_j is the hit rate of the j th pixel.

324 The efficiency requirement on the bandwidth and the hit rate becomes: $B_{W,i} > \mu_i$, where the
325 index i means the constraint is for a single pixel; if all the N pixels on a column have the same
326 rate $\mu = N\mu_i$, the condition reduces to $B_W > \mu$. The bandwidth must be chosen such that the
327 mean time between hits of the last pixel in the readout chain is bigger than that.

328 In order to reduce the bandwidth a readout with zero suppression on pixel is typically employed;
329 this means that only information from channels where the signal exceeds the discriminator thresh-
330 old are stored. Qualcosa sulla zero suppression? La metto qui questa affermazione?

331 If instead there is a local storage until a trigger signal arrives, the input rate to column bus
332 μ' is reduced compared to the hit rate μ as: $\mu' = \mu \times r \times t$, where r is the trigger rate and t is
333 the bunch crossing period. In this situation there is a more relaxed constraint on the bandwidth,
334 but the limiting factor is the buffer depth: the amount of memory designed depends both on the
335 expected rate μ and on the trigger latency t as $\propto \mu \times t$, that means that the higher the trigger
336 latency and the lower the hit rate to cope with.

337 In order to have an efficient usage of memory on pixels' area it's convenient grouping pixels
338 into regions with shared storage. Let's compare two different situations: in the first one a buffer
339 is located on each pixel area, while in the second one a core of four pixels share a common buffer
340 (this architecture is commonly called FE-I4).

341 Consider a 50 kHz single pixel hits rate and a trigger latency of 5 μs , the probability of losing

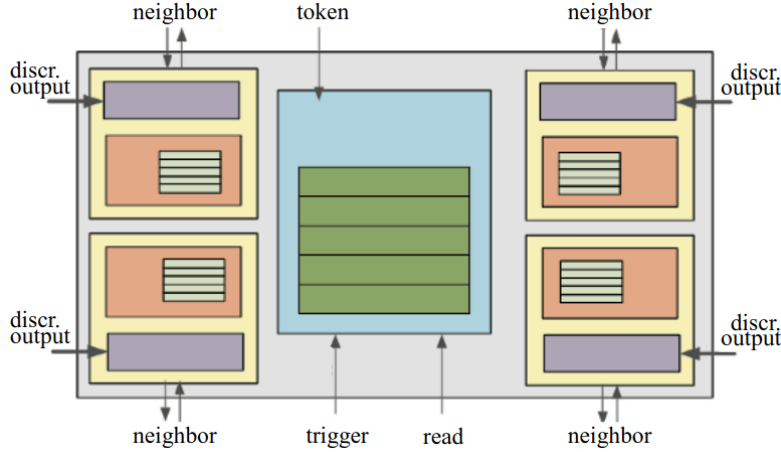


Figure 2.10: Block diagram of the FE-I4 R/O. Read and memory management section is highlighted in light blue; latency counters and trigger management section are highlighted in green; hit processing blocks are highlighted in purple; ToT counters and ToT management units are highlighted in orange

³⁴³ hits is:

$$P(N > 1|\nu) = 1 - P(N = 0|\nu) - P(N = 1|\nu) = 1 - e^{-\nu}(1 + \nu) \approx 2.6\% \quad (2.10)$$

³⁴⁴ where I have assumed a Poissonian distribution with mean $\nu = 0.25$ to describe the counts N.

³⁴⁵ To get an efficiency ϵ greater than 99.9 % a 3 hit depth buffer is needed:

$$P(N > 3|\nu) = 1 - \sum_{i=0}^3 P(N = i|\nu) < 0.1\% \quad (2.11)$$

³⁴⁶ Considering the second situation: if the average single pixel rate is still 50 kHz, grouping four pixels
³⁴⁷ the mean number of hits per trigger latency is $\nu = 0.25 \times 4 = 1$. To get an efficiency of 99.9% (eq.
³⁴⁸ 2.11) a buffer depth of 5 hits in the four-pixels region, instead of 3 per pixels, is needed.

³⁴⁹ Chapter 3

³⁵⁰ Use of pixel detectors

³⁵¹ There always was a tight relation between the development of cameras and pixel detectors since
³⁵² 1969, when the idea of CCDs, thanks to whom Boyle and Smith were awarded the Nobel Prize in
³⁵³ Physics in 2009, revolutionized photography allowing light to be captured electronically instead of
³⁵⁴ on film. Even though the CMOS technology was already known when CCDs spread, the costs of
³⁵⁵ productions were too high to allow the diffusion of these sensors for which needed to wait until
³⁵⁶ 1990s. From that period on, the fast diffusion of CMOS was mainly due to the less cost than
³⁵⁷ CCD, and the less power required for supply. Nowadays CCDs are still preferred over MAPS in
³⁵⁸ astronomy, where the astronomical sources' rate are low enough to cope with tens of ms for the
³⁵⁹ readout.

³⁶⁰ The principal use cases of pixel detectors are particle tracking and imaging: in the former case
³⁶¹ individual charged particles have to be identified, in the latter instead an image is obtained by
³⁶² the usually un-triggered accumulation of the impinging radiation. Also the demands on detectors
³⁶³ performance depends on their usage, in particular tracking requires high spatial resolution, fast
³⁶⁴ readout and radiation hardness.

³⁶⁵ 3.1 Tracking in HEP

³⁶⁶ At first the physics world overlooked the CCDs, and all pixel in general, as against the gaseous
³⁶⁷ detector for tracking: there was no need to replace these ones which had a sufficient good resolution
³⁶⁸ ($100\text{ }\mu\text{m}$). Since 1974, with the measurement of the invariant mass of the **j psi** and the affirmation
³⁶⁹ of the quark model, all experiments start to look for better spatial resolutions in order to achieve
³⁷⁰ the possibility of reconstructing short lived particle.

³⁷¹ Historically, the first pixel detector employed in particle physics was a CCD: it was installed in
³⁷² the spectrometer at the CERN's Super Proton Synchrotron (SPS) by the ACCMOR Collaboration
³⁷³ (Amsterdam, CERN, Cracow, Munich, Oxford, RAL) at mid 1980s, with the purpose of studying
³⁷⁴ the recently-discovered charm particles. The second famous usage of CCDs took place at SLAC
³⁷⁵ in the Large Detector (SLD) during the two years 1996-98. **Cosa vedono di così importante da**
³⁷⁶ **dire che servono i pixel detector?** From that period on particle tracking in experiments have been
³⁷⁷ transformed radically: it was mandatory for HEP experiments to build an inner vertex detector.
³⁷⁸ In 1991, the more demanding environments led to the development of hybrid pixel detectors:
³⁷⁹ a dedicated collaboration, RD19, was established at CERN with the specific goal to define a
³⁸⁰ semiconductor micropattern detector with an incorporated signal processing at a microscopic level.
³⁸¹ In those years a wide set of prototypes of hybrid pixel has been manufactured; among the greatest
³⁸² productions a mention goes to the huge ATLAS and CMS vertex detectors. From the middle of
³⁸³ 2013 a second collaboration, RD 53, has been established with the new goal to find a pixel detector
³⁸⁴ suitable for phase II future upgrades of those experiments. Even if the collaboration is specifically
³⁸⁵ focused on design of hybrid pixel readout chips (aiming to 65 nm technique so that the electronics
³⁸⁶ fits within the pixel area), also other options have been taken in account and many test have been
³⁸⁷ done on MAPS for example. Requirements imposed by HL-LHC will become tighter in time: for
³⁸⁸ example, a dose and radiation of 5 Mrad and 1016 NIEL are expected after 5 years of operation.
³⁸⁹ Time resolution, material budget and power consumption are also issues for the upgrade: a time
³⁹⁰ resolution better than 25 ns for a bunch crossing frequency of 40 MHz, a material budget lower
³⁹¹ than 2% and a power consumption lower than 500 mW/cm^2 are required.

392 Amidst the solutions proposed 3D silicon detector, invented by Sherwood Parker in 1995, and
393 MAPS are the most promising. In 3D sensors the electrode is a narrow column of n-type implanted
394 vertically across the bulk instead of being implanted on the wafer's surface. The charge produced
395 by the impinging particle is then drifted transversally within the pixel, and, as the mean path
396 between two electrode can be sufficient low, the trap probability is not an issue. 3D pixels have
397 been already proved in ATLAS tracker [quando?](#). Even if 3D detector are adequately radiation hard,
398 MAPS architecture looked very promising from the beginning: they overcome both the CCDs long
399 reading time and the hybrid problems (I have already explained in section ?? the benefits of
400 MAPS). Experiments such as ALICE at LHC and STAR at RHIC have already introduced the
401 CMOS MAPS technology in their detectors. ALICE Tracking System (ITS2), upgraded during the
402 LHC long shut down in 2019-20, was the first large-area ($\sim 10 \text{ m}^2$ covered by 2.5 Gpixels) silicon
403 vertex detector based on CMOS MAPS.

404 3.1.1 Hybrid pixels at LHC and at SuperKEKB

405 ATLAS

406 With CMS, ATLAS is one of two general-purpose detectors at the LHC and has the largest volume
407 detector ever constructed for a particle collider (46 m long and 25 m in diameter). The Inner
408 Detector consists of three different systems all immersed in a magnetic field parallel to the beam
409 axis whose main components are: the pixel, the micro-strips and transition radiation trackers.
410 Concerning the pixel detector, 92 million pixels are divided in 4 barrel layers and 3 disks in each
411 end-cap region, covering a total area of 1.9 m^2 and having a 15 kW of power consumption.

412 As stated by the ATLAS collaboration the pixel detector is exposed by an extreme particle
413 flux: "By the end of Run 3¹, the number of particles that will have hit the innermost pixel layers
414 will be comparable to the number it would receive if it were placed only a few kilometres from
415 the Sun during a solar flare". Considering that the particle density will increase even more with
416 HL-LHC, radiation hardness is definitively target to achieve.

417 The most ambitious goal is employ a MAPS-based detector for the inner-layer barrels, and for
418 this reason the RD53 collaboration is performing many test on MAPS prototypes, as Monopix of
419 which I will talk about in section ??.

420 Up to now this possibility will be eventually implemented during the second phase of the HL-
421 LHC era, as at the start of high-luminosity operation the selected option is the hybrid one. The
422 sensor will be bonded with ITkPix, the first full-scale 65 nm hybrid pixel-readout chip developed
423 by the RD53 collaboration. Regarding the sensor, a valueable option is using 3D pixels, which
424 have already proved themselves in ATLAS, for the insertable B layer (IBL).[qualcosa in più sui 3d.](#)
425 The number of pixels will be increased of a factor about 7, passing from 92 milions to 6 billion.

426 CMS

427 [da scrivere](#) 124 million pixels; cylindrical layers roughly at 3cm, 7cm, 11cm and 16cm and disks at
428 either end, and so will be vital in reconstructing the tracks of very short-lived particles. Each of
429 these silicon pixels is 100um by 150um,even with only around 50 microwatts per pixel, the total
430 power output is 7.5kW-

431 LHCb

432 LHCb is a dedicated heavy-flavour physics experiment that exploits pp interactions at 14 TeV at
433 LHC. It was the last experiment to upgrade the vertex detector, the Vertex Locator (VELO),
434 replacing the silicon-strip with pixels in May 2022. As the instantaneous luminosity in Run3 is
435 increased by a factor $\lesssim 10$, much of the readout electronics and of the trigger system have been
436 developed in order to cope with the large interaction rate. To place the detector as close as possible
437 to the beampipe and reach a better track reconstruction resolution, the VELO has a surprising
438 feature: it can be moved. During the injection of LHC protons it is parket at 3 cm from the beams
439 and only when the stability is reach it is brought at ~ 5 mm. Radiation hardness as well as readout
440 speed are then a priority for the detectors: that's why the collaboration opted for a hybrid system.
441 The Velopix is made bonding sensors, each measuring 55×55 micrometers, $200 \mu\text{m}$ -thick to a
442 $200 \mu\text{m}$ -thick ASIC specially developed for LHCb and coming from the Medipix family (sec. ??),

¹Run 3 start in June 2022

443 which can handles hit rates up to 900 MHz per chip. Since the detector is operated under vacuum
444 near the beam pipe, the heat removal is particularly difficult and evaporative CO₂ microchannel
445 cooling are used.

446 **BelleII**

447 The current vertex detector of BelleII, VXD, is made of a pixel detector (PXD), fabricated with
448 2 layers of DEPFET-based pixels, and 4 layers of a double-sided silicon strip detectors (SVD)[5].
449 Due to the small capacitance of the collection node, DEPFET presents a high signal-to-noise ratio
450 (in 30-50) thanks to the low intrinsic noise and to the large signal achieved with the fully depleted
451 bulk: pixels are thinned to 75 μm in the active region, then a MIP is supposed to create a signal of
452 $\sim 6000 \text{ e}^-$, while the typical noise of DEPFET is around 200 e^- . **The ASIC read out is still based
453 on a rolling shutter logic, with an integration time of 20 μs .** In order to reduce the data-storage
454 memory PXD hits are only used to improve spatial resolution of tracks: the SVD informations are
455 used by the High Level Trigger (HLT) to look for regions of interest in the pixel ladders just by
456 extrapolating back the tracks found in the tracker detector, and this method allows to store only
457 data belonging to these areas; the PXD hits are then used in offline track fit to improve the vertex
458 resolution.

459 MAPS have been proposed for the replacement of VXD during the Long Shut Down 2 (LSD2)
460 foreseen around 2026-27; the new vertex detector, VTX, should be made of 5 layers fabricated
461 by the optimized Belle II pixel sensor (OBELIX), a detector based on TJ-Monopix have been
462 selected (look at chapter ??). The main advantages VTX should bring are a obvious improving
463 in the track and vertex resolution (14 μm before upgrade, $\lesssim 10 \mu\text{m}$ expected after upgrade) and a
464 reduction in the X_0 (**da.. a..**), a higher background tolerance because of the smaller sensor than
465 strips dimension and a low bandwidth due to the on-chip sparsification.

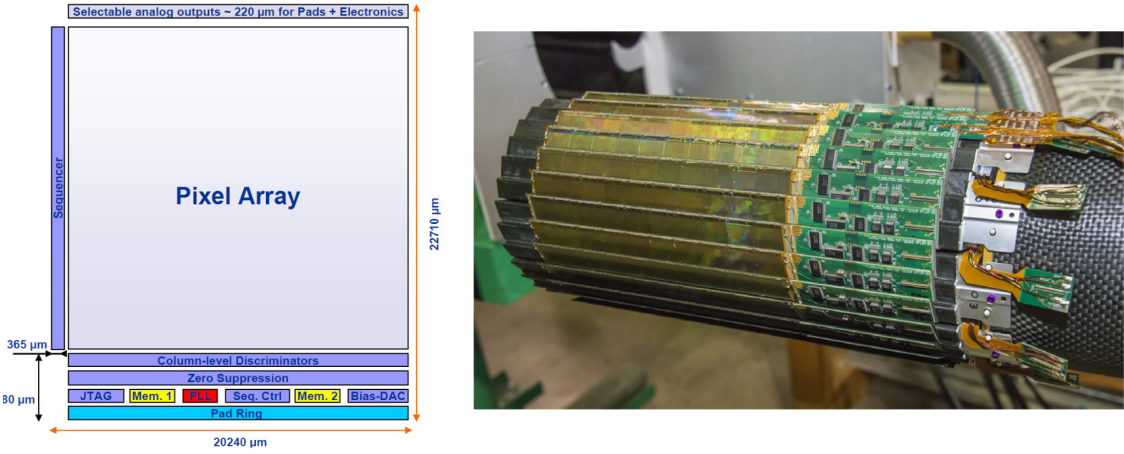
466 **3.1.2 First attempts to MAPS**

467 **MIMOSA at EUDET and STAR**

468 MIMOSA [6][7] (standing for Minimum Ionizing MOS Active pixel sensor), designed in 2008,
469 prefigured the architecture of MAPS for coming vertex detector being the first large scale sensor
470 to be employed as detector. MIMOSA-26 equipped the final version of EUDET high resolution
471 beam telescope both at CERN-SPS and at DESY while the MIMOSA-28 devices are used for
472 the first MAPS-based vertex detector at the STAR experiment. MIMOSA-26 is fabricated in a
473 350 nm, and a module features 1152 columns, split into 18 independent groups, and 576 rows, with
474 square pixels having a side of 18.4 μm length; therefore, because of the small dimension, charge
475 sharing is an issue **aggiungi qualcosa**. The readout is done in a rolling shutter mode: the chip is
476 an Active Pixels (APS) and therefore it incorporates the amplification on pixel, while the signal
477 discrimination and zero-suppression logic are placed at the EoC, where is also placed a memory.
478 The chip is an Active Pixels (APS) and therefore it incorporates the amplification on pixel, while
479 the signal discrimination and zero-suppression logic are placed at the EoC: the readout is done in
480 a rolling shutter mode with a frame integration time that can be lowered down to 85 ms, and a
481 memory allowing to store up to six hits is.

482 The EUDET telescope, equipped with six sensor planes, requires highly granular and thin pixel
483 detectors in order to achieve an excellent track resolution (around 2 μm) even at the rather low
484 particle energies of up to 6 GeV. The STAR experiment at the Relativistic Heavy Ion Collide
485 (RHIC) accelerator at the Brookhaven National Laboratory (BNL) is the first to include MAPS
486 in the vertex detector[8]. The main tracking detector in STAR is a TPC with radii 60-190 cm
487 embedded in a 0.5 T solenoidal magnetic field, that provides a pointing resolution of approximately
488 1 mm. The pixel detector, PXL, is a part of a 3-detector system, Heavy Flavor Tracker (HFT), that
489 has been added to the pre-existing STAR apparatus just before the 2014 Run in order to improve
490 the impact parameter resolution and to enable the direct reconstruction of hadronic decays of heavy
491 flavor mesons and baryons. The Heavy Flavor Tracker (HFT) is composed by the Silicon Strip
492 Detector (SSD), the Intermediate Silicon Tracker (IST) and the Pixel Detector (PXL); the first
493 one is placed at 22 cm from the beam pipe and consists of double sided strips with 95 μm inter-strip
494 pitch, the second one, placed at 14 cm, is made of single sided silicon pads with 600 $\mu\text{m} \times 6 \text{ mm}$ pitch
495 and the last one made by two layers is placed at 2.8 cm and 8 cm fabricated with ULTIMATE2 (also
496 known as MIMOSA-28), a successor of MIMOSA-26 sensor, with pitch 20.7 μm and thinned down

497 to 50 μm . An area of 0.16 m^2 are covered by 400 MAPS sensor, corresponding to 356 millions of
 498 pixels divided into array size of 928×960 . Each pixel includes circuitry for readout, amplification,
 499 and Correlated Double Sampling (CDS) for signal extraction and noise subtraction and the frame
 500 integration time is $185.6 \mu\text{s}$; after the subtraction the signal to noise ratio is ~ 30 , with a noise
 501 between 10-12 electrons and a signal of 1000 e^- . Thanks to the HFT system and the PXL, STAR
 502 achieved a track pointing resolution $46 \mu\text{m}$ for $750 \text{ MeV}/c$ kaons, and better than $30 \mu\text{m}$ for particle
 503 momenta bigger than $1 \text{ GeV}/c$: this performance enabled the study of D-meson production with a
 high significance signal.



504 Figure 3.1: (a) The HFT PXL detector; (b) Block-diagram of the ULTIMATE-2 sensor

505 ALPIDE at ALICE

506 ALICE (A Large Ion Collider Experiment) is a detector dedicated to heavy-ion physics and to the
 507 study of the condensed phase of the chromodynamics at the LHC. The tracking detector consists of
 508 the Inner Tracking System (ITS), the gaseous Time Projection Chamber (TPC) and the Transition
 509 Radiation Detector (TRD), and all those are embedded in a magnetic field of 0.5 T. The ITS is
 510 made by six layers of detectors, two for each type, from the interaction point outwards: Silicon
 511 Pixel Detector (SPD), Silicon Drift Detector (SDD) and Silicon Strip Detector (SSD). Contrary
 512 to the others LHC experiments, ALICE tracker in placed in a quite different environments: the
 513 expected dose is smaller by two order of magnitude and the rate of interactions is few MHz instead
 514 of 40 MHz, but the number of particles comes out of each interaction is higher (the SPS is invested
 515 by a density of particles of $\sim 100 \text{ cm}^{-2}$). The reconstruction of very complicated events whit a large
 516 number of particle is a challenge, hence to segment and to minimize the amount of material, which
 517 may cause secondary interaction complicating futher the event topology, is considered a viable
 518 strategy. The detector employes the ALPIDE chip, developed by ALICE collaboration, fabricated
 519 in the 180 nm CMOS Imaging Sensor process of TowerJazz, whose design takes full advantage of
 520 process feature which allows full circuitry within the pixel matrix. Thanks to the reduction of the
 521 material budget, ITS2 obtained an amazing improvement both in the position measurement and
 522 in the momentum resolution, improving the efficiency of track reconstruction for particle with very
 523 low transverse momentum (by a factor 6 at $pT \sim 0.1 \text{ GeV}/c$). Further advancements in CMOS
 524 MAPS technology are being aggressively pursued for the ALICE ITS3 vertex detector upgrades
 525 (foreseen around 2026-27), with the goals of further reducing the sensor thickness and improving
 526 the readout speed of the devices, while keeping power consumption at a minimum.

527 3.2 Other applications

528 Historically for imaging pourpose the CCDs were the favoured device: they can be used as single
 529 photon counter or integrating and collecting the charge released by more impinging particles. The
 530 utilisation in the first case is similar to the tracking one, except that the requirements are less
 531 tight, so much that two noteworthy of microchips originally meant for detectors in particle physics
 532 at the LHC, and later employed in other fields are Medipix and Timepix. They are read-out chips

533 developed by the Medipix Collaborations since early 1990s. For two decades, different Medipix
534 generations have been produced, having a rough correlation with the feature size used: Medipix2
535 (1999) used 250 nm feature size CMOS while Medipix3 (2005) 130 nm. The aim of the fourth col-
536 laboration (2016), instead, is designing pixel read-out chips that prepared for TSV processing and
537 may be tiled on all four sides. **DOVREI METTERE DUE RIGHE SU TSV OPPURE TAGLIARE.**

538 For photons imaging other materials with higher atomic charge than silicon could be prefered,
539 as a high photon absorption efficiency is needed: it was for this reason that Medipix2 was bump
540 bonded to identically segmented sensors of both silicon and GaAs.

541 The applications in scientific imaging vary from astrophysics and medical imaging to more exotic
542 domains as studies of protein dynamics, art authentication and dosimetry. The most important
543 employment of Medipix is as X-ray single photon counting in industrial and medical radiography
544 and in 3D computed tomography. Thanks to a New-Zealand company, the MARS Bioimaging
545 detector has been fabricated, which is capable of resolving the photons energy and produce 3D
546 coloured images. Besides tracking in HEP (I have already cited the use of Timepix3 is in the beam
547 telescope of the LHCb VELO), an important use of Timepix is in dosimetry **Timepix Detector**
548 **for Imaging in Ion Beam Radiotherapy- aggiungi qualche info** A small-Timepix detector with the
549 dimension of a USB can also be found at the International Space Station, where it is exploited for
550 radiation, principally made of heavy-ion, monitoring.

551 3.2.1 Applicability to FLASH radiotherapy

552 A possible new application of pixels detector is dosimetry or beam monitoring of charge particles in
553 high intensity radiography. The radiological treatment is a common method used in 60% of tumors
554 both as palliative care and as treatment. It can be given before, after or during a surgery, (Intra
555 operative radiation therapy-IORT) and many different types of radiations (photons, electrons,
556 protons and ions, which mainly are hydrogen and carbon) can be used to irradiate the affected
557 tissues. Exploiting the ionizing energy loss, that can be parametrized by the Linear Energy
558 Transfer (LET), a biological damage can be delivered to the tissue: while α and β particles are
559 high LET radiations with values in $100 \text{ keV}/\mu\text{m}$ to $200 \text{ keV}/\mu\text{m}$, x-rays and gamma-rays are low
560 LET radiations with values in range $0.2 \text{ keV}/\mu\text{m}$ to $2 \text{ keV}/\mu\text{m}$.

561 If x-ray photons, with energy in 4 MeV to 25 MeV are used, the ionization is caused by the
562 Compton electrons and is more in the superficial layers of the tissue due to the exponential attenu-
563 ation of the beam. The hadrons energy loss, instead, is strongly localized in the last region of the
564 track, that is the Bragg peak. Ion beam enables better focusing of the radiation thereby improves
565 the sparing of the surrounding healthy tissues; on the other hand the delivered dose distribution
566 depends more on the patient's density tissues (e.g. bones, swelling, fat). **Ensuring the target**
567 **coverage is a fundamental objective in radiotherapy and is closely connected to the choice of the**
568 **particles.** Electrons cover the target since they tend to spread out and can cover a field size of a few
569 cm^2 at a distance of a few cm from the source. Instead, the limited size of the beam for protons
570 and photons from ultra high dose rate microbeam radiation therapy (MRT), for which FLASH
571 effect was seen, requires the scanning of target. The radiobiological consequences of scanning both
572 in spatial-fractionation and in prolonged exposure, which might not be sufficient to maintain a
573 high mean dose rate to trigger FLASH effect, need to be explored. To date, the FLASH effect has
574 been most commonly demonstrated using low-energy electron linacs

575 Recently² a promising method for RT at ultra high dose rate (at least 40 Gy/s) and for this
576 reason called FLASH-RT[9], instead of CONV-RT (0.03 Gy/s), came out. This treatment takes
577 advantages of biological differences between tumors and healthy tissues: it is characterized by
578 reducing normal tissue toxicity and maintaining equivalent tumor damage. The response to dose
579 can be described by the survival fraction probability, describing the fraction of surviving cell as a
580 function of the dose:

$$S(D) = S(0) e^{-(\alpha D + \beta D^2)} \quad (3.1)$$

581 where α and β respectively represents the rate of cell killing by single ionizing events and by
582 double hits. Hence, at high doses the density of damages increases and the cells repair becomes
583 more difficult. Even if the FLASH effect is not yet completely understood and the underlying
584 mechanisms are not clear, it looks like there are two different recipes which are involved:

²The first evidences has been observed on mice experiments in 1966 and in 2014 by the group of Favaudon and Vozenin. After this, many test on cats and pigs have been performed, and also there has been a clinical trial on a cutaneous tumor-patient

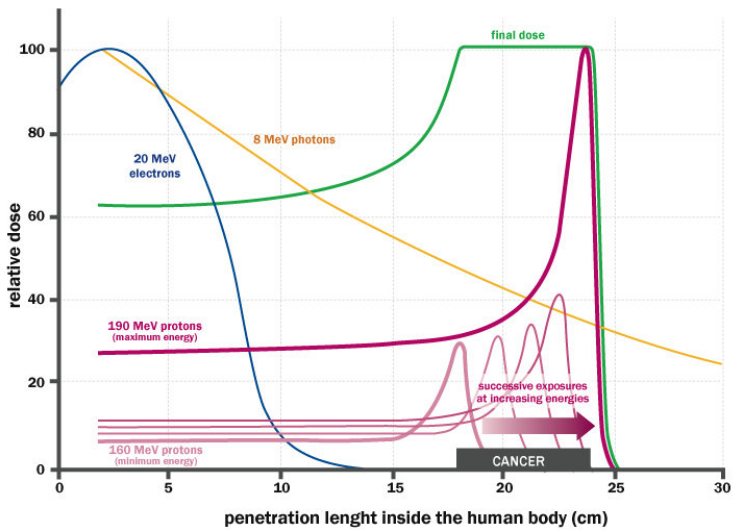


Figure 3.2: The Spread Out Bragg Peak (SOBP) curve (green), which is a constant dose distribution, is obtained from the superposition of many Bragg peak of hadrons with different energy.

	CONV-RT	FLASH-RT
Dose rate	0.03 Gy/s	40 Gy/s
Intra pulse dose rate	100 Gy/s	106 Gy/s
Treatment duration	~minutes	$\lesssim 500$ ms
DDP	0.3 mGy	1 Gy to 10 Gy
Pulse width	3 μ s	~ 2 μ s

Table 3.1: Typical value of treatment parameters

- 585 • **The dose rate:** higher dose rate produce bigger damages (fig. 3.3(a)) since this prevent
586 cells from sparing.
- 587 • **The presence or absence of oxygen:** while hypoxic cells are very resistant to radiation,
588 normal oxygenated cells are highly radiosensitive. This is because if molecules containing O_2
589 break due to the impinging radiation, then the oxygen can build Reactive Oxygen Species
590 (ROS) (fig.3.3(b))

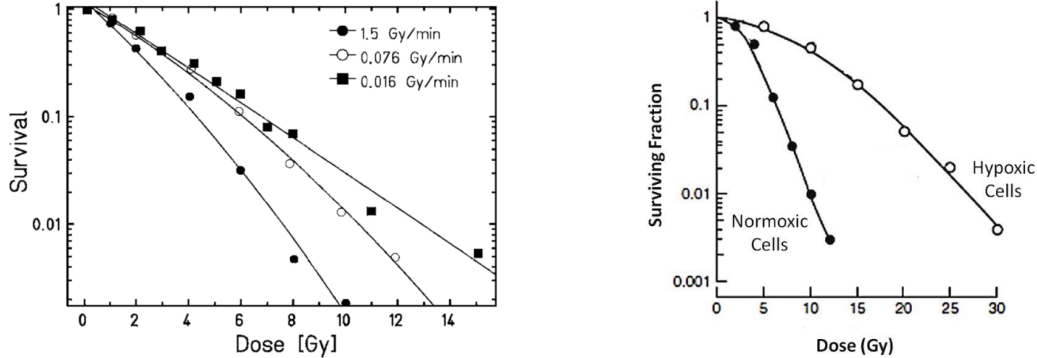


Figure 3.3: (a) Survival curve for different dose rate and (b) for different oxygen cell content

591 The Tumor Control Probability (TCP) and the Normal Tissue Complication (NTC) functions
592 parametrize respectively the efficiency of damaging on the tumor after having released a certain
593 dose and the probability of not affecting the healthy tissues. The intermediate zone between the
594 increase of the TC and of the NTC is called therapeutic window, and the wider it is and the more
595 effective the treatment is.

596 Dosimetric problems

597 Finding dosimeters suitable for online monitoring of the beam at ultra high dose rate is still an
598 open issue since almost all standard online dosimeters show saturation problems. Differently,
599 radiochromic films, which are the standard passive dosimeters, show dose-rate independence up to
600 109 Gy/s. **Cosa sono i radiochromic films and they do not have the same accuracy of other detectors.**
601 The principal detectors for reference dosimetry which provide real-time dose measurement are
602 Ionization Chambers (IC), that show saturation issue at dose per pulse (DDP) two orders of
603 magnitude lower than the ones used for FLASH-RT. **da qui in poi** ICs devono essere calibrate
604 secondo la metrologia , per cui grazie a protocolli di calibrazione e introducendo dei fattori correttivi
605 si riesce a fare una misura di dose. k_{sat} which accounts for the loss of charge collected due to
606 recombination. Doppi problemi sia di saturazione dovuta a ion recombination sia di scariche, must
607 be carefully accounted for: questo doppio effetto è dato dal fatto che, creandosi tante cariche nella
608 camera, che va ad annullare il campo elettrico di drift. Questo ovviamente paralizza le cariche che
609 non driftano più, ma che anzi si ricombinano ed inoltre facilita la formazione di scariche. Per DDP
610 minori di 1 mGy il fattore correttivo è minore al 5%, poi però aumenta substantially.

611 Scintillators have reusable, non-exhaustible scintillation centers. However, the system has a
612 total deadtime given by both the crystal scintillation time and the electronics read-out deadtime.

613 Semiconductors show a nonreversible saturation beyond a threshold around 15 cGy/p. The
614 scintillator used, shows a negligible saturation up to 1 Gy/p, but it increases significantly up to at
615 least 11 Gy/p, and it reaches a cutoff value between 11 and 36 Gy/p.

616 Scintillator dosimeters are widely used in radiotherapy. They are usually operating in counting-
617 mode where each detected signal is processed by read-out electronics. However, the system has a
618 total deadtime given by both the crystal scintillation time and the electronics read-out deadtime
619 When a scintillator dosimeter is used in integrator-mode the signal is integrated over the entire
620 irradiation time. A deadtime, due to the decay time of the scintillating material, is considered on
621 average every N recorded pulses, where N is the number of scintillation centres in the dosimeter.

622 Besides saturation two other requirements for online dosimeters are high temporal and space res-
623 olutions. **Si potrebbe pensare di poter usare i pixel detector as beam monitor che hanno risoluzioni**
624 **spaziali anche inferiori al 10 um e ris temporali -qua dare un valore è più difficile perchè per i**

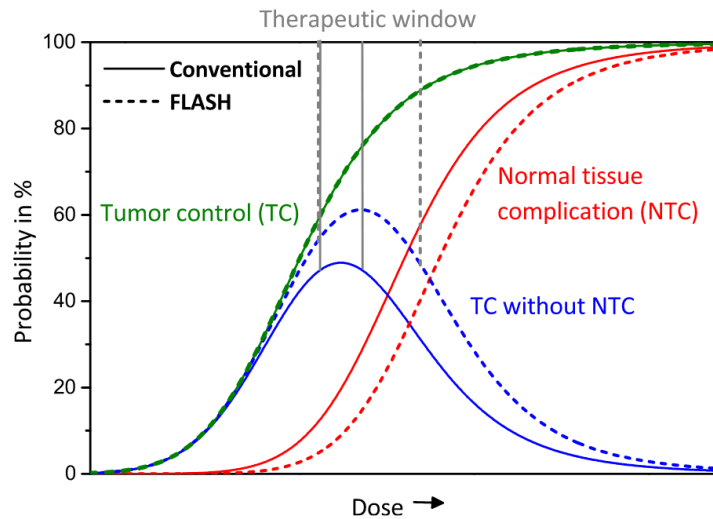


Figure 3.4: Illustration of dependence of TCP, NTCP and therapeutic window on dose, for CONV-RT ad FLASH-RT.

625 maps la risoluzione temporale dipende da l occupancy. Uno dei problemi è però il lungo dead time
 626 introdotto dal lungo tempo di readout (ricorrdiamo che sopportano circa 100 Mhz/cm²).

⁶²⁷ **Chapter 4**

⁶²⁸ **TJ-Monopix1**

⁶²⁹ TJ-Monopix1 is a small electrode DMAPS with fast R/O capability, fabricated by TowerJazz
⁶³⁰ foundry in 180 nm CMOS imaging process. It is part, together with prototypes from other series
⁶³¹ such as TJ-MALTA, of the ongoing R&D efforts aimed at developing DMAPS in commercial CMOS
⁶³² processes, that could cope with the requirements at accelerator experiments. Both TJ-Monopix
⁶³³ and TJ-MALTA series [10], produced with the same technology by TowerJazz (the timeline of the
⁶³⁴ foundry products is shown in figure 4.1), are small electrode demonstrators and principally differ in
⁶³⁵ the readout design: while Monopix implements a column-drain R/O, an asynchronous R/O without
⁶³⁶ any distribution of BCID has been used by TJ-Malta in order to reduce power consumption.



Figure 4.1: Timeline in TowerJazz productions in 180 nm CMOS imaging process

⁶³⁷ Another Monopix series, but in 150 nm CMOS technology, has been produced by LFoundry [11].
⁶³⁸ The main differences between the LF-Monopix1 and the TJ-Monopix1 (summarized in table 4.2),
⁶³⁹ lay in the sensor rather than in the readout architecture, as both chips implements a fast column
⁶⁴⁰ drain R/O with ToT capability [12][13]. Concerning the sensors, either are based on a p-type
⁶⁴¹ substrate, but with slightly different resistivities; in addition LFoundry pixels are larger, thicker
⁶⁴² and have a large fill factor (the very deep n-well covers ~55% of the pixel area). The primary
⁶⁴³ consequence is that LF-Monopix1 pixels have a higher capacity resulting in higher consumption
⁶⁴⁴ and noise. As I discussed in section 2.4.1, the fact that LF-Monopix has a large fill factor electrode
⁶⁴⁵ is expected to improve its radiation hardness. Indeed, a comparison of the performance of the
⁶⁴⁶ two chips showed that TJ-Monopix suffers a comparatively larger degradation of efficiency after
⁶⁴⁷ irradiation, due to the low electric field in the pixel corner; on the other hand, a drawback of the
⁶⁴⁸ large fill factor in LF-Monopix is a significant cross-talk.

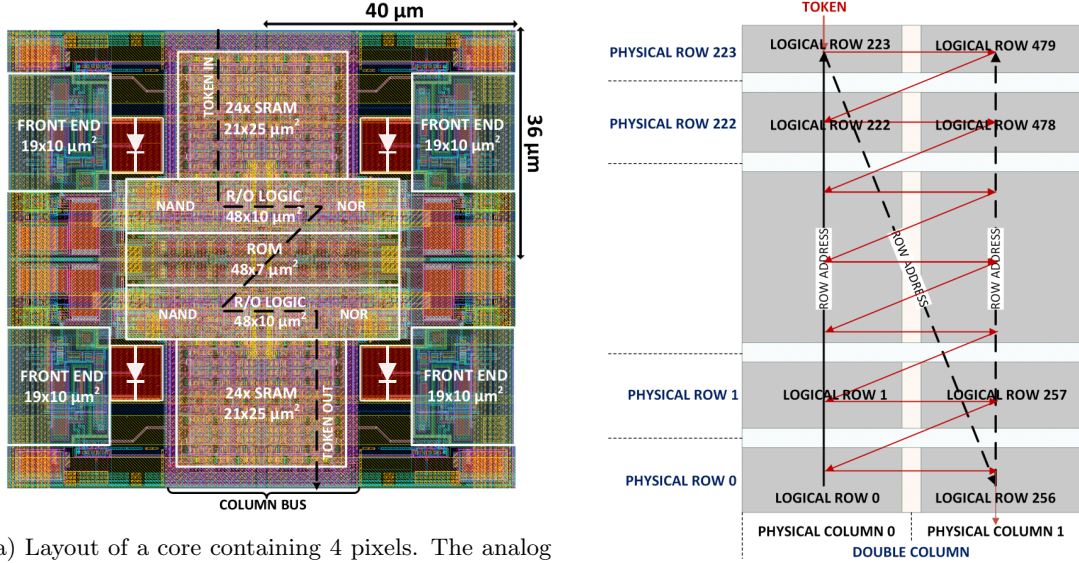
⁶⁴⁹ The TJ-Monopix1 chip contains, apart from the pixels matrix, all the required support blocks
⁶⁵⁰ used for configuration and testing:

- ⁶⁵¹ the whole matrix contains 224×448 pixels, yielding a total active area approximately equal
⁶⁵² to 145 mm^2 over a total area of $1 \times 2 \text{ cm}^2$;
- ⁶⁵³ at the chip periphery are placed some 7-bit Digital to Analog Converter (DAC), used to
⁶⁵⁴ generate the analog bias voltage and current levels and to configure the FE;

	LF-Monopix1	TJ-Monopix1
Resistivity	$>2\text{ k}\Omega\text{cm}$	$>1\text{ k}\Omega\text{cm}$
Pixel size	$50 \times 250\mu\text{m}^2$	$36 \times 40\mu\text{m}^2$
Depth	$100\text{-}750\mu\text{m}$	$25\mu\text{m}$
Capacity	$\sim 400\text{ fF}$	$\sim 3\text{ fF}$
Preamplifier	charge	voltage
Threshold trimming	on pixel (4-bit DAC)	global threshold
ToT	8 bits	6 bits
Consumption	$\sim 300\text{ mW/cm}^2$	$\sim 120\text{ mW/cm}^2$
Threshold	$1500 e^-$	$\sim 270 e^-$
ENC	$100 e^-$	$\sim 30 e^-$

Table 4.1: Main characteristics of Monopix1 produced by TowerJazz and LFoundry [12][13]

- at the EoC is placed a serializer to transferred datas immediately, indeed no trigger memory is implemented in this prototypes;
 - the matrix power pads are distributed at the sides
 - four pixels which have analog output and which can be monitored with an oscilloscope, and therefore used for testing
- Pixels are grouped in 2×2 cores (fig. 4.2a): this layout allows to separate the analog and the digital electronics area in order to reduce the possible interference between the two parts. In addition it simplifies the routing of data as pixels on double column share the same column-bus to EoC. Therefore pixels can be addressed through the physical column/row or through the logical column/row, as shown in fig. 4.2b: in figure is also highlighted the token propagation path, whose I will discuss later.



(a) Layout of a core containing 4 pixels. The analog FE and the digital part are separated in order to reduce cross-talk be

(b)

4.1 The sensor

As already anticipated, TJ-Monopix1 has a p-type epitaxial layer and a n doped small collection electrode ($2\mu\text{m}$ in diameter); to avoid the n-wells housing the PMOS transistors competing for the charge collection, a deep p-well substrate, common to all the pixel FE area, is used. TJ-Monopix1 adopts the modification described in section 2.4.2 that allows to achieve a planar depletion region

Parameter	Value
Matrix size	$1 \times 2 \text{ cm}^2$
Pixel size	$36 \times 40 \mu\text{m}^2$
Depth	$25 \mu\text{m}$
Electrode size	$2 \mu\text{m}$
BCID	40 MHz
ToT-bit	6
Power consumption	$\sim 120 \text{ mW/cm}^2$

Table 4.2

671 near the electrode applying a relatively small reverse bias voltage. This modification improves the
 672 efficiency of the detector, especially after irradiation, however a simulation of the electric field in
 673 the sensor, made with the software TCAD (Technology Computer Aided Design), shows that a
 674 nonuniform field is still produced in the lateral regions of the pixel compromising the efficiency
 675 at the corner. Two variations to the process have been proposed in order to further enhance the
 676 transversal component of electric field at the pixel borders: on a sample of chip, which includes the
 677 one in Pisa, a portion of low dose implant has been removed, creating a step discontinuity in the
 678 deep p-well corner (fig. 4.3); the second solution proposed[MOUSTAKAS THESYS, PAG 58]
 679 consists in adding an extra deep p-well near the pixel edge. A side effect of the alteration in the
 680 low dose implant is that the separation between the deep p-well and the p-substrate becomes weak
 681 to the point that they cannot be biased separately to prevent the punchthrough.

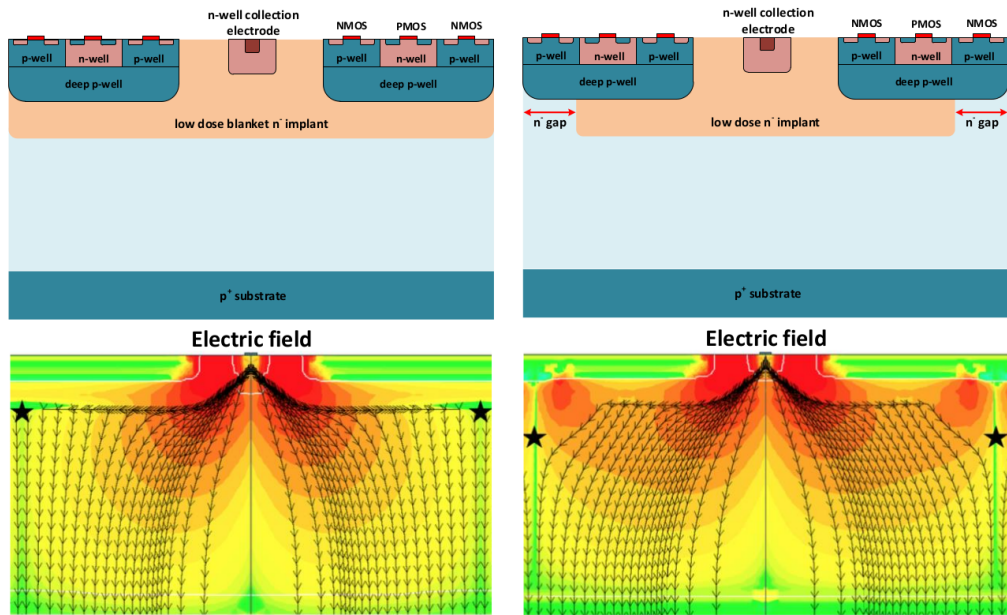


Figure 4.3: (a) The cross-section of a monolithic pixel in the TJ-Monopix with modified process; additionally in (b) a gap in the low dose implant is created to improve the collection of charge due to a bigger lateral component of the electric field. this point in figure is indicated by a star . transversal component of the electric field drops at the pixel corner

682 Moreover, to investigate the charge collection properties, pixels within the matrix are split
 683 between bottom top half and bottom half and feature a variation in the coverage of the deep
 684 p-well: the electronics area can be fully covered or not. In particular the pixels belonging to rows
 685 from 0 to 111 are fully covered (FDPW) and pixels belonging to rows from 112 to 223 have a
 686 reduced p-well (RDPW), resulting in a enhancement of the lateral component of the electric field.

4.2 Front end

The matrix is split in four sections, each one corresponding to a different flavor of the FE. The four variation have been implemented in order to test the data-bus readout circuits and the input reset modes.

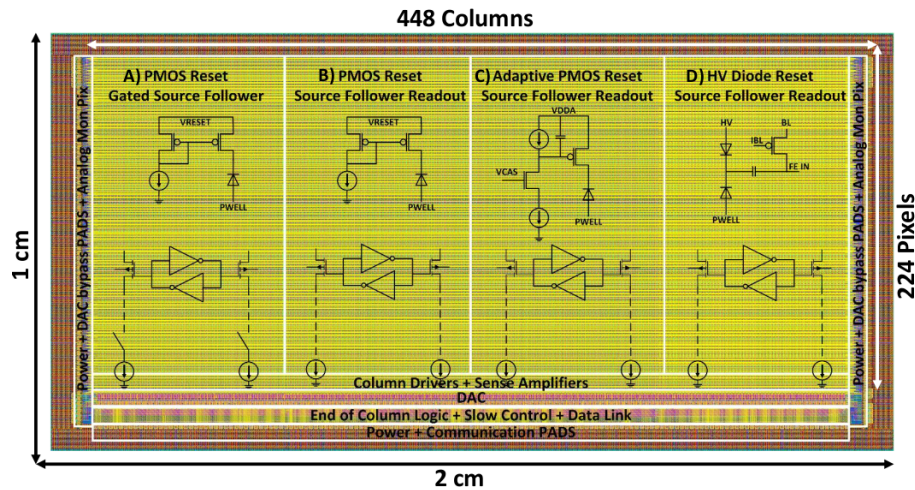


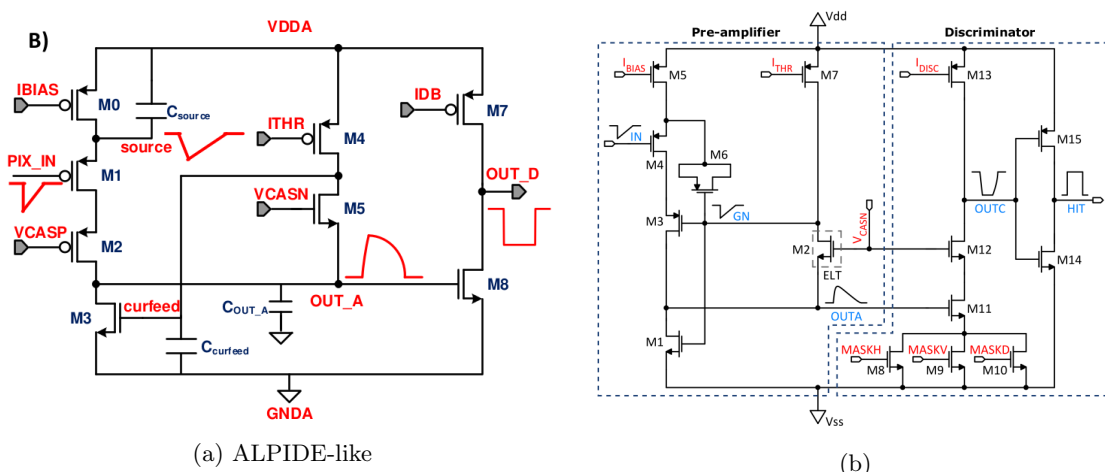
Figure 4.4

All the flavors implement a source-follower double-column bus readout: the standard variation is the flavor B, that features a PMOS input reset (referred as "PMOS reset"). Flavor A is identical to flavor B except for the realization of the source follower (it is a gated one) that aim to reduce the power consumption. cosa significa? C instead implements a novel leakage compensation circuit. Moreover the collection electrode in flavors A, B, C is DC-coupled to the front-end input, while in D is AC-coupled, providing to apply a high bias voltage; for this reason flavor D is called "HV flavor".

Principio generale: R resistenza di reset deve essere abbastanza grande in modo da far sì che il ritorno allo zero è abbastanza lento (non devi "interferire" con la tot slope e non deve essere più corto del tempo del preamplificatore, sennò hai perdita di segnale). Baseline reset: all'input solitamente hai un PMOSS o un diodo; R reset

4.2.1 ALPIDE-like

ALPIDE chips, developed by the ALICE collaboration, implemented a standard FE to the point that many CMOS MAPS detectors used a similar FE and are called "ALPIDE-like". Considering that both TJ-Monopix1 and ARCADIA-MD1 have an ALPIDE-like FE, I am going to explain the broad principles of the early FE stage. The general idea is of the amplification to transfer the



Parameter	Meaning	
IBIAS	mainly controls the rise time	yes? check
IDB	sets the discriminator threshold	yes
ITHR	sets the velocity of the return to the baseline	yes
ICASN	sets the baseline of the signal	yes
VRESET	sets the gain of the preamplifier	yes
IRESET	sets the gain of the preamplifier	no

Table 4.3: FE parameters which must be setted through the DAQ. "Function" means that higher parameter implies higher value

707 charge from a bigger capacity[14], C_{source} , to a smaller one, C_{out} : the input transistor M1 with
 708 current source IBIAS acts as a source follower and this forces the source of M1 to be equal to the
 709 gate input $\Delta V_{PIX_IN} = Q_{IN}/C_{IN}$.

$$Q_{source} = C_{source} \Delta V_{PIX_IN} \quad (4.1)$$

710 The current in M2 and the charge accumulates on C_{out} is fixed by the one on C_{source} :

$$\Delta V_{OUT_A} = \frac{Q_{source}}{C_{OUT_A}} = \frac{C_{source} \Delta V_{PIX_IN}}{C_{OUT_A}} = \frac{C_{source}}{C_{OUT_A}} \frac{Q_{IN}}{C_{IN}} \quad (4.2)$$

711 A second branch (M4, M5) is used to generate a low frequency feedback, where VCASN and ITHR
 712 set the baseline value of the signal on C_{OUT_A} and the velocity to goes down to the baseline.

IL RUOLO DI CURVFEED NON L'HO CAPITO.

713 Finally IDB defines the charge threshold with which the signal OUT_A must be compared: de-
 714 pending on if the signal is higher than the threshold or not, the OUT_D is high or low respectively.

715 The actual circuit implemented in TJ-Monopix1 is shown in figure 4.5b: the principal difference
 716 lays in the addition of disableing pixels' readout. This possibility is uttermost important in order to
 717 reduce the hit rate and to avoid saturating the bandwidth due to the noisy pixels, which typically
 718 are those with manufacturing defects. In the circuit transistors M8, M9 and M10 have the function
 719 of disabling registers with coordinates MASKH, MASKV and MASKD (respectively vertical, ori-
 720 ginal and diagonal) from readout: if all three transistors-signals are low, the pixel's discriminator
 721 is disabled. Compared with a configurable masking register which would allow disableing pixels
 722 individually, to use a triple redundancy reduces the sensistivity to SEU but also gives amount of
 723 intentionally masked ("ghost") pixels. This approach is suitable only for extremely small number
 724 N of pixel has to be masked: if two coordinate projection scheme had been implemented, the
 725 number of ghost pixels would have scale with N^2 , if instead three coordinates are used, the N's
 726 exponential is lower than 2 (fig. 4.6)

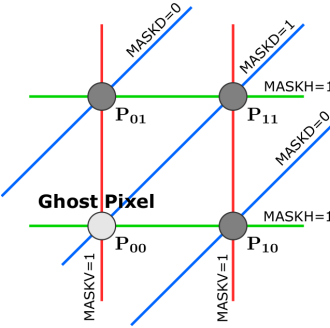


Figure 4.6

727

4.3 Readout logic

728 TJ-Monopix1 has a triggerless, fast and with ToT capability R/O which is based on a column-drain
 729 architecture. On the pixel are located two Random Access Memory (RAM) cells to store the 6-bit

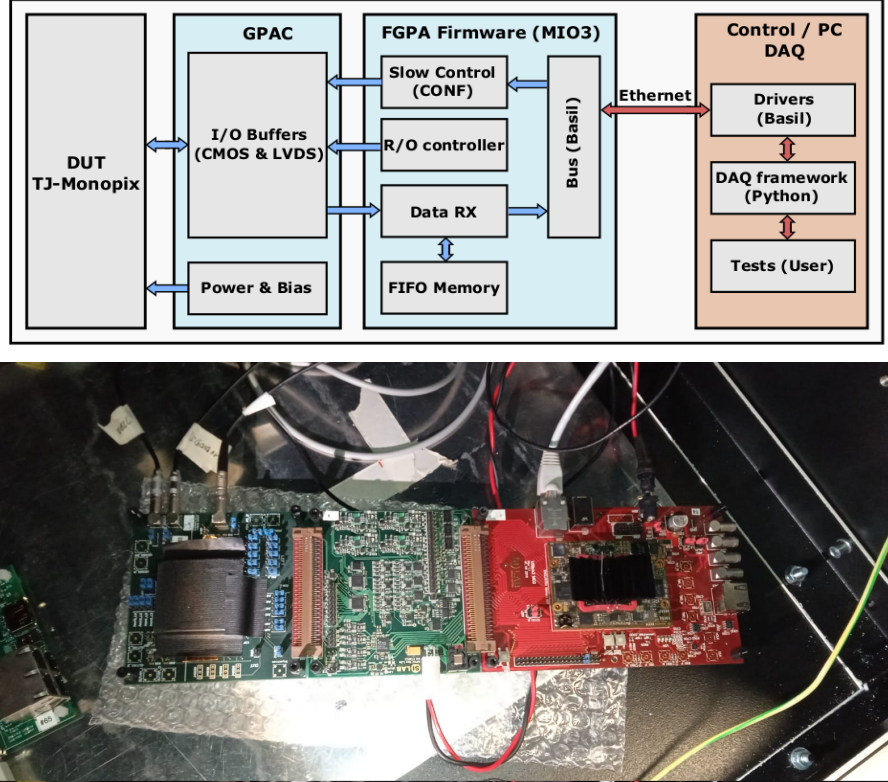


Figure 4.7: Main caption

731 LE and 6-bit TE of the pulse, and a Read-Only Memory (ROM) containing the 9-bit pixel address.
 732 Excluded these memories, TJ-Monopix1 hasn't any other buffer: if a hit arrives while the pixel is
 733 already storing a previous one, the new data get lost. After being read, the data packet is sent to
 734 the EoC periphery of the matrix, where a serializer transfers it off-chip to an FPGA (4.7). There
 735 a FIFO is used to temporarily stored the data, which is transmitted to a computer through an
 736 ethernet cable in a later time.

737 The access to the pixels' memory and the transmission of the data to the EoC, following
 738 a priority chain, is managed by control signals and is based on a Finite State Machine (FSM)
 739 composed by four state: no-operation (NOP), freeze (FRZ), read (RD) and data transfer (DTA).
 740 The readout sequence (??) starts with the TE of a pulse: the pixel immediately tries to grab the
 741 column-bus turning up a hit flag signal called *token*. The token is used to control the priority chain
 742 and propagates across the column indicating what pixel that must be read. To start the readout
 743 and avoid that the arrival of new hits disrupt the priority logic, a *freeze* signal is activated, and
 744 then a *read* signal controls the readout and the access to memory. During the freeze, the state of
 745 the token for all pixels on the matrix remains settled: this does not forbid new hits on other pixels
 746 from being recorded, but forbids pixels hit from turning on the token until the freeze is ended. The
 747 freeze stays on until the token covers the whole priority chain and gets the EoC: during that time
 748 new token cannot be turned on, and all hits arrived during a freeze will turn on their token at the
 749 end of the previous freeze. Since the start of the token is used to assign a timestamp to the hit,
 750 the token time has a direct impact on the time resolution measurement; this could be a problem
 751 coping with high hits rate.

752 The analog FE circuit and the pixel control logic are connected by an edge detector which is
 753 used to determine the LE and the TE of the hit pulse(fig. 4.9): when the TE is stored in the first
 754 latch the edge detector is disabled and, if the **FREEZE** signal is not set yet, the readout starts. At
 755 this point the HIT flag is set in a second latch and a token signal is produced and depending on
 756 the value of **Token in** the pixel can be read or must wait until the **Token in** is off. In figure an OR
 757 is used to manage the token propagation, but since a native OR logic port cannot be implemented
 758 with CMOS logic, a sum of a NOR and of an inverter is actually used; this construct significantly
 759 increases the propagation delay (the timing dispersion along a column of 0.1-0.2 ns) of the token

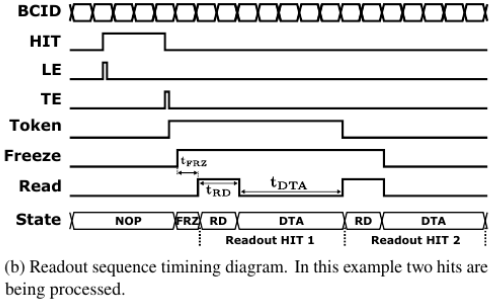


Figure 4.8: Readout timing diagram: in this example two hits are being processed

and to speed up the circuit optimized solution are often implemented. When the pixel become the next to be read in the queue, and at the rising edge of the **READ** signal, the state of the pixel is stored in a D-latch and the pixel is allowed to use the data bus; the TE and the HIT flag latches are reset and a **READINT** signal that enable access of the RAM and ROM cells is produced.

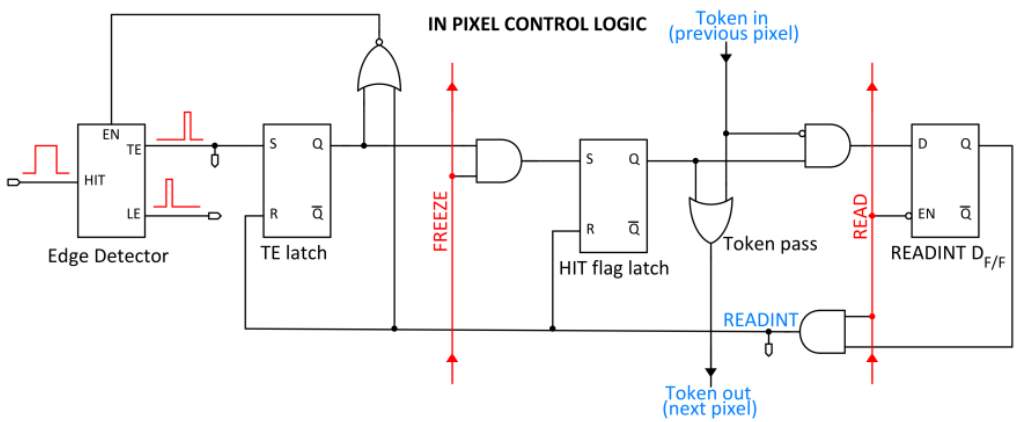


Figure 4.9

The final data must provide all the hits' information: the pixel address, the ToT and the timestamp. All those parts are assigned and appended at different time during the R/O chain:

- **Pixel address:** while the double column address (6-bit) is appended by the EoC circuit, the row address (8-bits for each flavor) and the physical column in the doublet (1-bit) are assigned by the in-pixel logic
- **ToT:** is obtained offline from the difference of 6-bits TE and 6-bits LE, stored by the edge detector in-pixel; since a 40 MHz BCID is distributed across the matrix, the ToT value is range 0-64 clock cycle which corresponds to 0-1.6 μ s
- **Timestamp:** The timestamp of the hit correspond to the time when the pixel set up the token; it is assigned by the FPGA, that uses the LE, TE and a 640 MHz clock to derive it. For all those hits which arrived while the matrix is frozen, the timestamp is no more correlated with the time of arrival of the particle

When the bits are joined up together the complete hit data packet is 27-bit.

4.3.1 Dead time measurements

The hit loss is due to analog and digital pile up: the first one occurs when a new hit arrives during the pre-amplifier response, the second instead, which is the more relevant contribution with high rate, while the information of the previous hit has not yet been transferred to the periphery. As only one hit at a time can be stored on the pixel's RAM, until the data have completed the path to get out, the pixel is paralyzed and the dead time τ almost corresponds with the time needed

Parameter	Value [DAC]	Value [μs]
START_FREEZE	64	1.6
STOP_FREEZE	100	2.5
START_READ	66	1.65
STOP_READ	68	1.7

Table 4.4: Default configuration of the R/O parameters

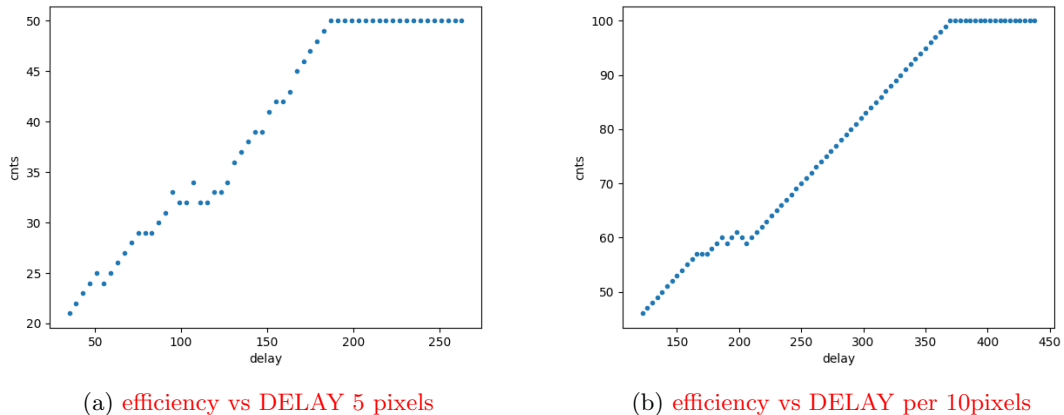
784 to trasmit the data-packets off-chip. Since the exportation of data from pixel to the EoC occurs
 785 via a 21-bits data bus, only one clock cycle is need to transfer the data to the end of column and
 786 the dead time bottleneck is given by the bandwidth of the serializer at the EoC. In our setup the
 787 serializer operates at 40 MHz, thus to transmit a data packet (27-bit considering the addition at
 788 the EoC) at least 675 ns are needed. For what we have said so far, the R/O is completely sequential
 789 and therefore is expected a linear dependence of the reading time on the number of pixels to read:

$$\tau = 25 \text{ ns} \times (\alpha N + \beta) \quad (4.3)$$

790 where α and β are parameters dependent on the readout chain setting.

791 To measure and test the linearity of the reading time with the number of pixels firing, I have
 792 used the injection mode available on the chip. Indeed, the injection mode allows fixing not only
 793 the amplitude of the pulse, which corresponds to the charge in DAC units, but also the period and
 794 the width. I have injected a fix number of pulses (100) and looked for the rate when the efficiency
 795 decreases. Moreover to test that there is no dependece of the digital readout time from the charge
 796 of the pulse, I have try to change the amplitude of the pulse injected, but the parameters found
 797 were consistent with the default configuration ones.

798 Al posto degli esempi con 5 e 10 pixels metterei un esempio dell'efficienza vs il periodo quando
 799 leggo un singolo pixel. Una cosa che volevo fare era anche provare a fissare la slope con cui
 l'efficienza scende: se la slope è uguale per tutti il readout diventa completamente predittivo.



(a) efficiency vs DELAY 5 pixels

(b) efficiency vs DELAY per 10pixels

800 While the single pixel reading time and the dead time do not depend on the position on the
 801 pixel matrix and are equal to 106 (46+60) clock counts within 1 clock count, on the other hand the
 802 τ depends on the pixel position on the matrix when more than one pixel are firing. In particular
 803 the priority chain goes from row 224 to row 0, and from col 0 to 112, that means the last pixels to
 804 be read is the one on the bottom right corner of the matrix.

805 In figure 4.12 is reported the reading time versus the number of pixels injected; the R/O
 806 parameters that control the reading time and their default values are reported on table ??.

807 The factor α , referring to eq. 4.3 is proportional to the difference (STOP_FREEZE - START_READ),
 808 while the offset β lies between 5 and 15 clock counts. Since through the injection a random hit rate
 809 on the matrix can't be simulated, as the coordinates of the pixels to inject must be specified, for
 810 convenience I used the pixels on the same column/row. No difference in the α and β coefficients
 811 has been observed between the two case.

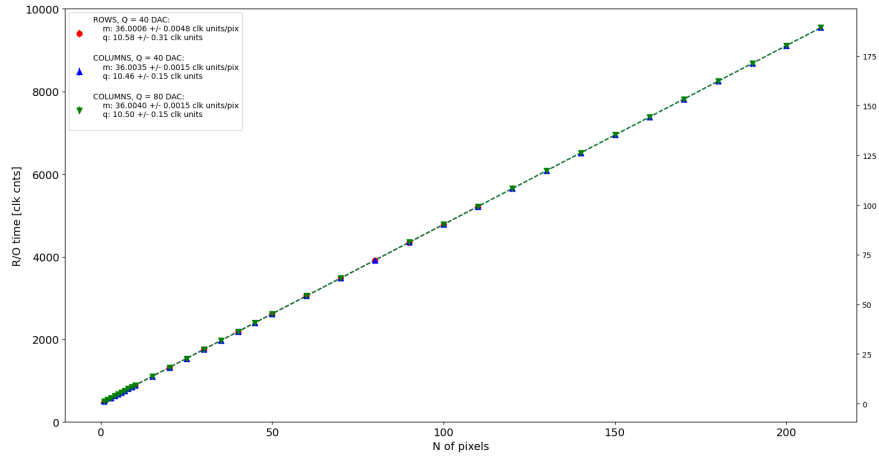


Figure 4.11

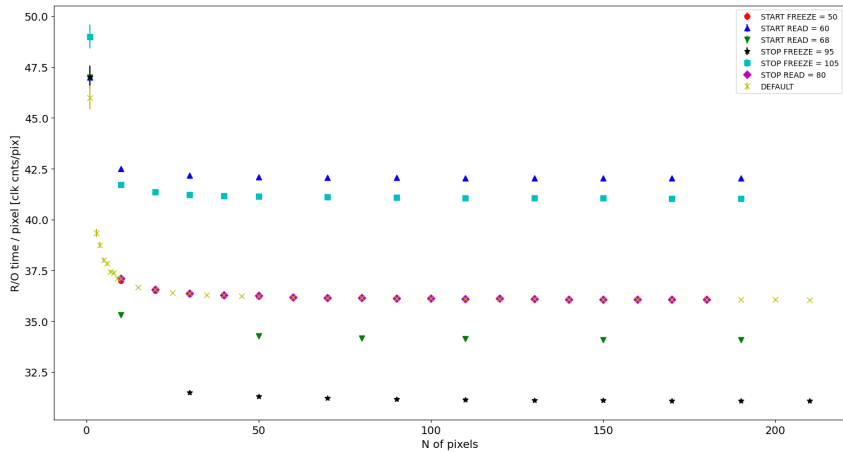


Figure 4.12

813 Ci sarebbe da spiegare perchè i parametri che usiamo noi come default non sono quelli che
 814 minimizzano il tempo di lettura. La spiegazione è che "Abbiamo copiato i valori dal repository
 815 di quelli di Bonn". Un'altra domanda potrebbe essere: come mai non ho esplorato una zona più
 816 vasta per i parametri del R/O. Cambiando molto i parametri del R/O la lettura non funzionava
 817 per niente: ad esempio CONF_STOP_FREEZE non può essere impostato né sopra 105 né sotto 95

818 4.4 Injection

- 819 • check sul chi quadro: fai un istogramma del chi quadro con fit retta e parabola
 820 • mappe dei parametri per un flavor

$$f(x, \mu, \sigma) = \frac{1}{2} \left(1 + erf \left(\frac{x - \mu}{\sigma\sqrt{2}} \right) \right) \quad (4.4)$$

$$erf(z) = \frac{2}{\sqrt{\pi}} e^{-z^2} dx \quad (4.5)$$

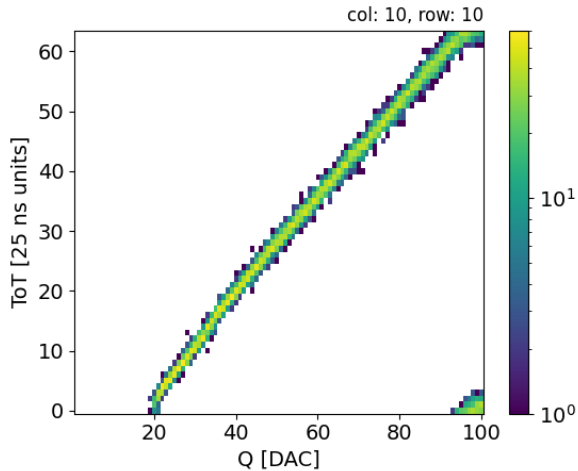
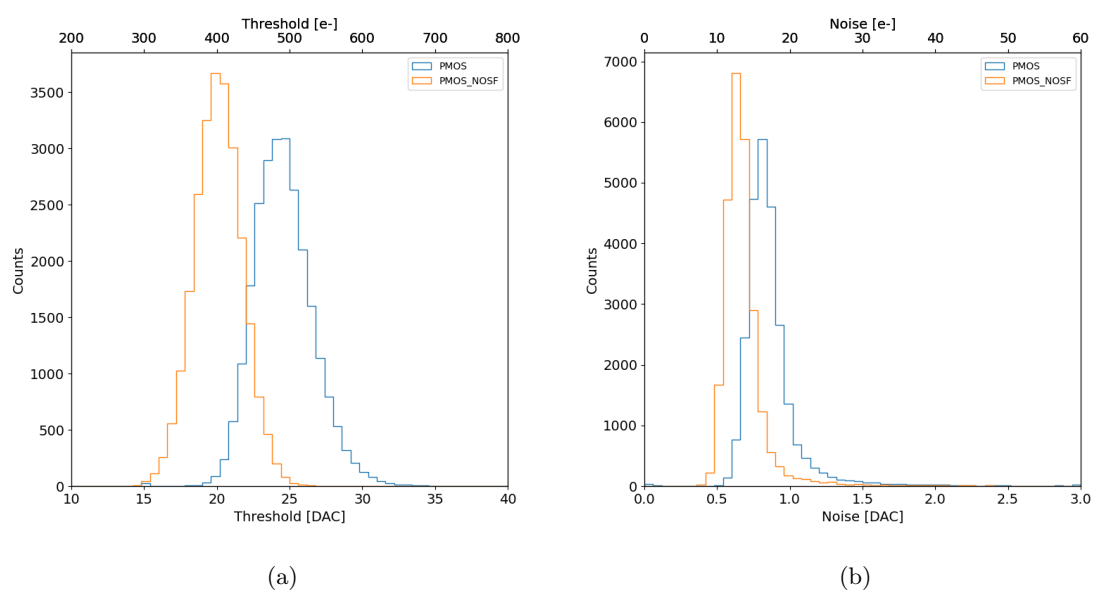
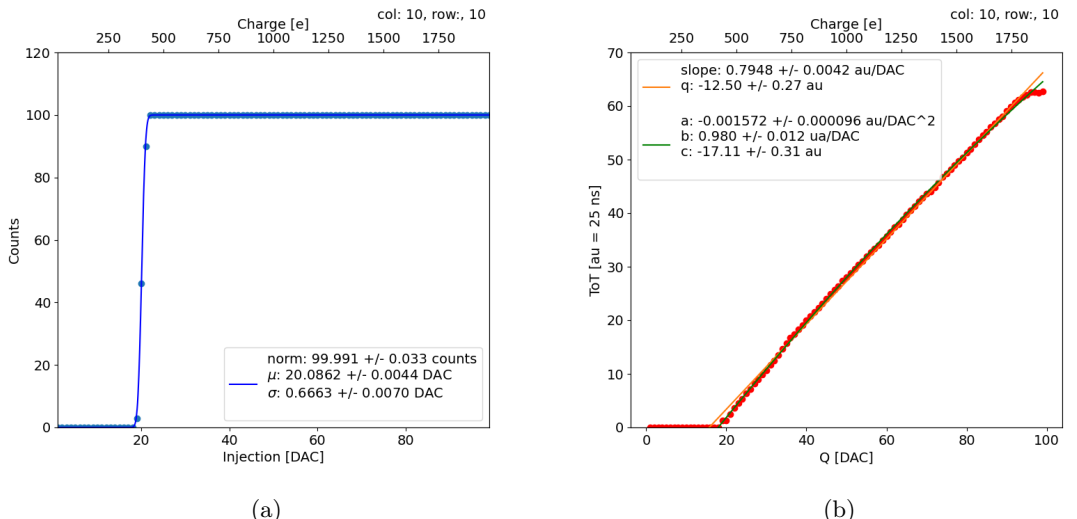
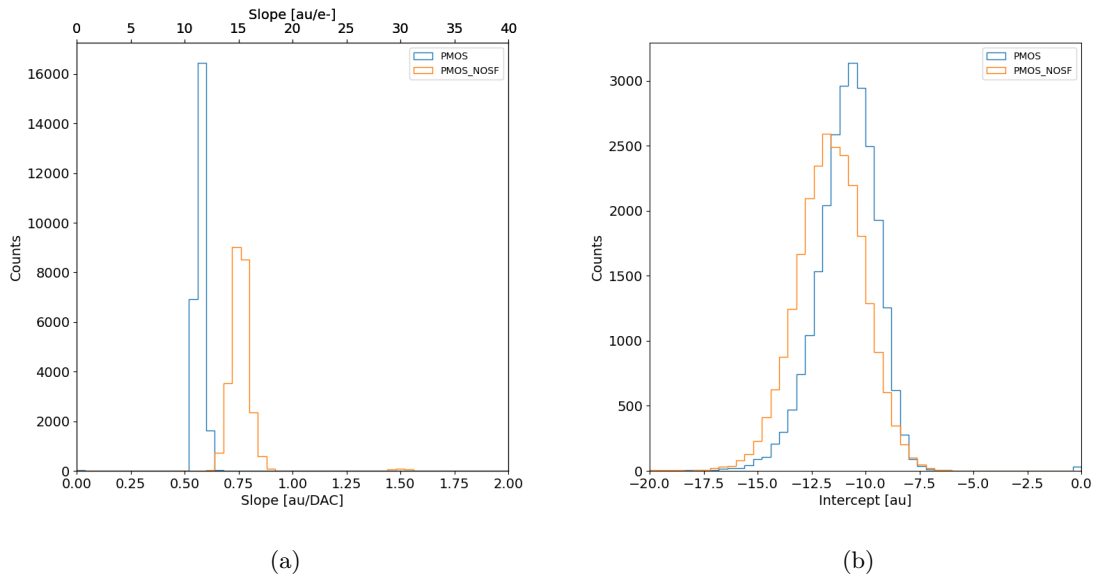


Figure 4.13: ToT rollover for pixel (10,10). The ToT is in range 0-64 since it is represented by 6 bit.





	DAC units	electrons
Threshold	24.529 ± 0.049 u: 24.433 ± 0.049 d: 24.623 ± 0.051	
Threshold dispersion	1.848 ± 0.033 u: 1.867 ± 0.034 d: 1.825 ± 0.035	
Noise	0.8222 ± 0.0043 u: 0.8225 ± 0.0045 d: 0.8221 ± 0.0043	
Noise dispersion	0.0975 ± 0.0030 u: 0.0968 ± 0.0031 d: 0.0970 ± 0.0030	

Table 4.5: Flavor PMOS

4.5 Measurements with radioactive sources

823 CI metterei i plot con ferro, stronzio e cosmici ToT con doppia scala (calibrata in elettroni e non
824 in ToT) hit per cluster dimensione cluster hit map di un paio di tracce?

825 4.6 Calibration of the ToT signal

826 calibrazione con il ferro Istogramma di singolo pixel del ferro Mappa dei parametri del fit sulla
827 matrice (media e sigma)

828 4.7 Fe vs bias

829 rate vs bias posizione del picco del ferro vs bias

	PMOS	HV
Slope [au/DAC]	0.57145 ± 0.00025	
Slope dispersion [au/DAC]	0.01685 ± 0.00016	
Intercept [au]	-10.824 ± 0.019	
Intercept dispersion [au]	1.225 ± 0.013	

Table 4.6

830 Chapter 5

831 Arcadia-MD1

832 [15] [16]

833 Breve introduzione analoga a Monopix1 in cui descrivo brevemente la "timeline" da SEED
834 Matisse a Md1 e Md2

835 5.1 The sensor

836 ARCADIA-MD1 is an LFoundry chip which implements the technology 110 nm CMOSS node
837 with six metal layer ???. The standard p-type substrate was replaced with an n-type floating zone
838 material, that is a tecnique to produce purified silicon crystal. (pag 299 K.W.).

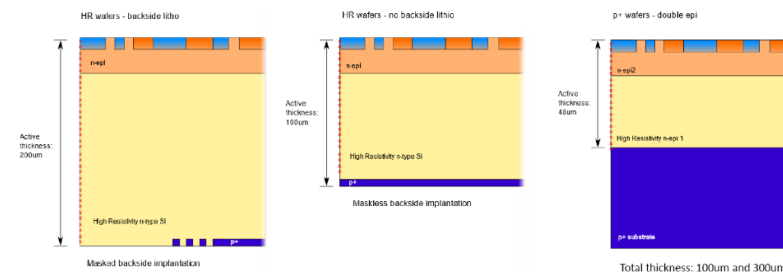


Figure 5.1

839
840 Wafer thinning and backside litography were necessary to introduce a junction at the bottom
841 surface, used to bias the substrate to full depletion while maintaining a low voltage at the front side.
842 C'è un deep pwell per - priority chainseparare l'elettronica dal sensore; per controllare il punchthrough
843 è stato aggiunto un n doped epitaxial layer having a resistivity lower than the substrate.

844 RILEGGI SUL KOLANOSKY COS'È IL PUNCHTHROUGHT, FLOAT ZONE MATERIAL,
845 COME VENGONO FATTI I MAPS COME FAI LE GIUNZIONI

846 It is part of the cathegory of DMAPS Small electrode to enhance the signal to noise ratio.
847 It is operated in full depletion with fast charge collection by drift.

848 Prima SEED si occupa di studiare le prestazioni: oncept study with small-scale test struc-
849 ture (SEED), dopo arcadia: technology demonstration with large area sensors Small scale demo
850 SEED(sensor with embedded electronic developement) Quanto spazio dato all'elettronica sopra il
851 pwell e quanto al diodo. ..

852 5.2 Readout logic and data structure

853 5.2.1 Matrix division and data-packets

854 The matrix is divided into an internal physical and logical hierarchy: The 512 columns are divided
855 in 16 section: each section has different voltage-bias + serializzatori. Each section is devided in

856 cores () in modo che in ogni doppia colonna ci siano 1Pacchetto dei dati 6 cores. ricordati dei serializzatori: sono 16 ma possono essere ridotti ad uno in modalità spazio

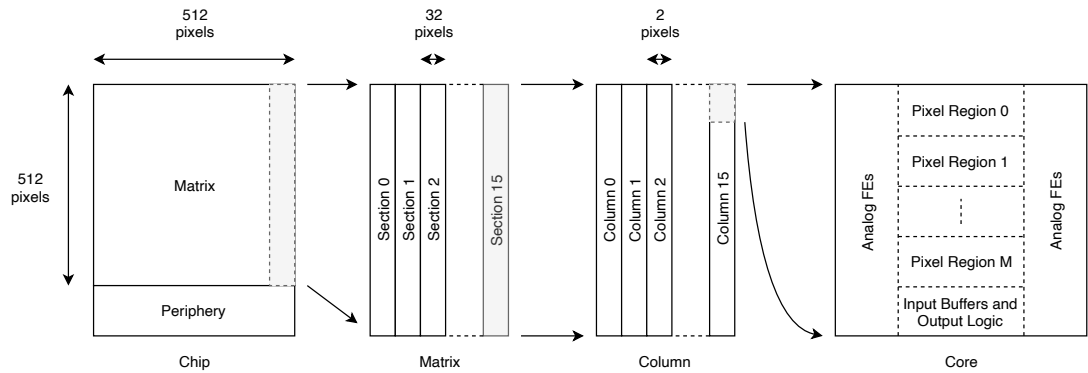


Figure 5.2

857

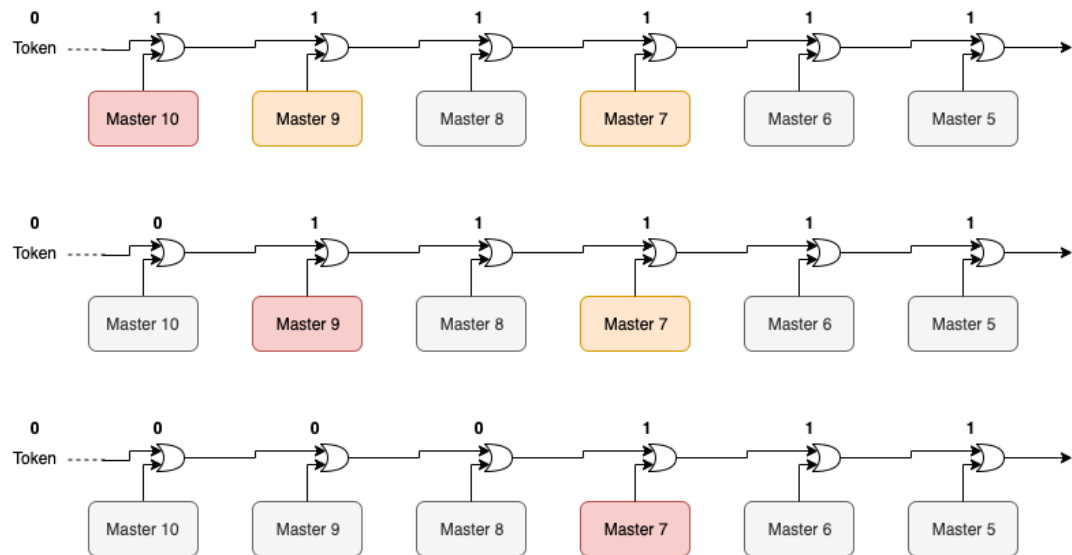


Figure 5.3

858 Questa divisione si rispecchia in come sono fatti i dati: scrivi da quanti bit un dato è fatto e le varie coordinate che ci si trovano dentro; devi dire che c'è un pixel hot e spieghi dopo a cosa serve, e devi accennare al timestamp
859
860

861 "A core is simply the smallest stepped and repeated instance of digital circuitry. A relatively
862 large core allows one to take full advantage of digital synthesis tools to implement complex func-
863 tionality in the pixel matrix, sharing resources among many pixels as needed.". pagina 28 della
864 review.

865

866 TABELLA: con la gerarchia del chip Matrix (512x512 pixels) Section (512x32 pixels) Column
867 (512x2) Core (32x2) Region (4x2)

868 Nel chip trovi diverse padframe: cosa c'è nelle padframe e End of section.

869 "DC-balance avoids low frequencies by guaranteeing at least one transition every n bits; for
870 example 8b10b encoding n =5"

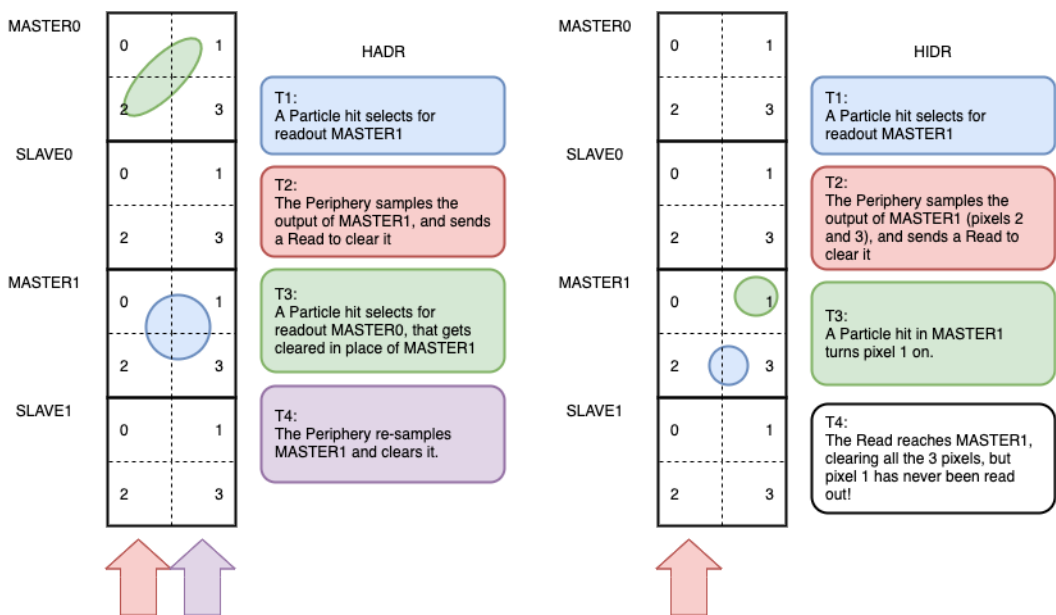


Figure 5.4

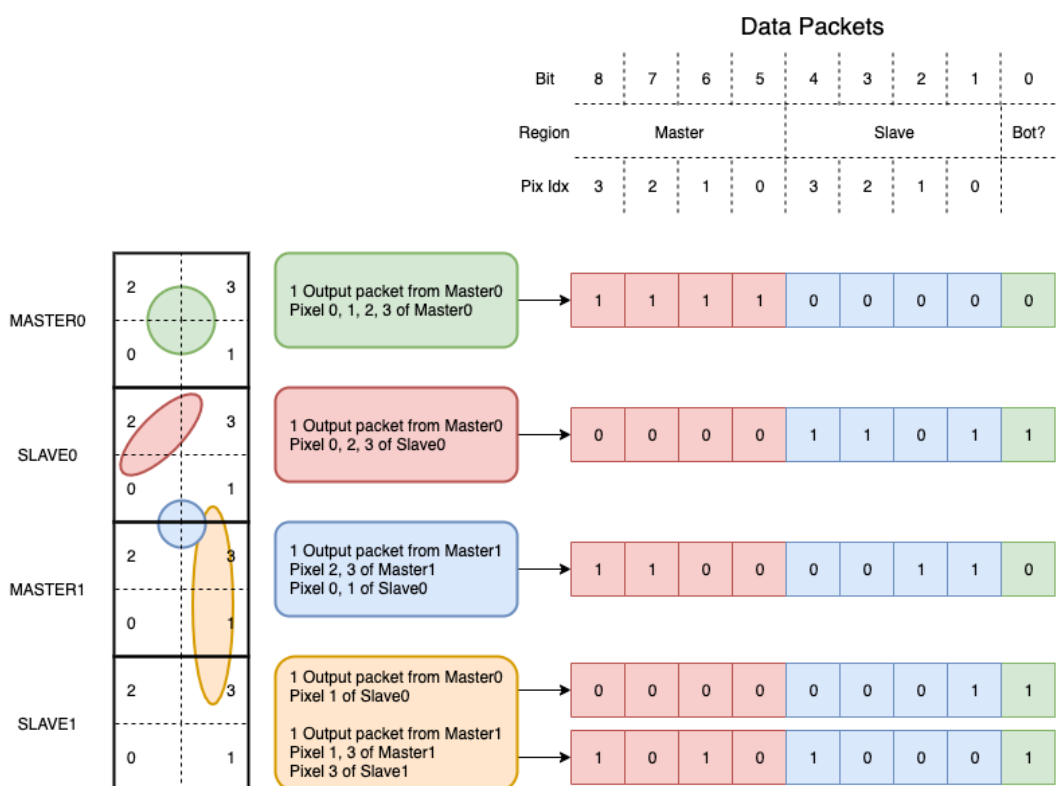


Figure 5.5

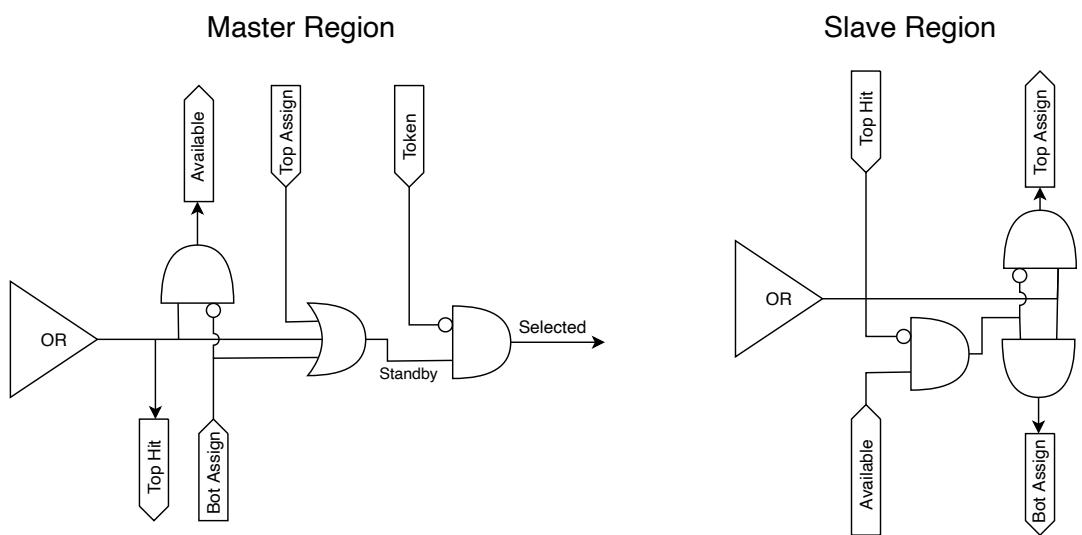


Figure 5.6

871 **Chapter 6**

872 **Threshold and noise
characterization**

874 **6.1 Threshold and noise: figure of merit for pixel detectors**

875 IN QUESTO CAPITOLO HO MESSO SOLO APPUNTI SPARSI DA RIORGANIZZARE, E
876 DEVO AGGIUNGERE POI I PLOT DI MONOPIX1

877 The threshold has to be high enough to cut the noise, but also low enough to mantain a high
878 signal efficiency, and For low enough threshold and/or enough pixels firing at the same time, this
879 positive feedback can set off a chain reaction causing all pixels to fire. For a given instantaneous
880 hit occupancy (fraction of pixels firing atthe same time due to an external stimulus), there will be
881 a minimum stable threshold. For this reason the signal to threshold ratio, rather than the signal
882 to noise ratio, can be considered as the figure of merit for pixel detectors.

883 la soglia è collegato al rumore, nel senso che: supponiamo di volere un occupancy di 10-4 allora
884 sceglierò la soglia in base a questo. (plot su quaderno) Da questo conto trovo la minima soglia
885 mettibile

886 In realtà quello che faccio è mettere una soglia un po' più grande perchè il rate di rumore dipende
887 da molti fattori quali la temperatura, l annealing ecc, e non voglio che cambiando leggermente uno
888 di questi parametri vedo alzarsi molto il rate di rumore. In realtà non è solo il rumore sensibile a
889 diversi fattori, ma anche la soglia: ad esempio la cosa classica è la variabilità della soglia da pixel
890 a pixel.

891 In questo modo rumore e soglia diventano parenti.

892

893 The front end noise does set a lower bound to the threshold, but does not determine how far
894 above this lower bound is the minimum stable threshold. Assuming a noise occupancy of 10meno4
895 is acceptable, this corresponds to the Gaussian 1-sided tail fraction for 3.7sigma . Inverting the
896 question, for a 500 e minimum threshold, the noise must be less than $500/3.7=135$ e equivalent
897 input charge. But this is just an upper bound. How far below this bound the noise needs to be
898 depends on how the threshold varies with time and how frompixel to pixel.

899 Questo implica tra le altre cose che voglio poter assegnare delle soglie diverse a diversi pixel.
900 Non fare trimming sulla soglia è uno dei problemi che si sono sempre incontrati: a casusa dei
901 mismatch dei transistor le soglie efficaci pixel per pixel cambiano tanto.

902 ASSEGNAZIONE DELLE SOGLIE IN TJ MONOPIX E ARAVDIA. Drawback è dare spazio
903 per registri e quantaltro. Ad esempio per Monopix1 la soglia è locale, poi 3 bit vengono allocati per
904 trimming sul singolo pixel. Arcadia invece Questo lascia però ancora aperto il problema tempo-
905 riale delle variazioni del rumore: problema per cui diventano necessarie le misure dei sensori dopo
906 l'irraggiamento.

907

908 La larghezza della s curve è il noise se assumi che il noise è gaussiano

909 Il trimming della soglia avviene con dei DAC: la dispersione della soglia dopo al tuning e dovuta
910 al dac è:

$$\sigma_{THR,tuned} = \frac{\sigma_{THR}}{2^{nbit}} \quad (6.1)$$

911 dove il numero di bit cambia varia tra 3-7 tipicamente. Monopix è 7 Arcadia 6

912 Each ROIC is different in this respect, but in general the minimum stable threshold was around
913 2500 electrons (e) in 1st generation ROICs, whereas it will be around 500 e for the 3rd generation.
914 This reduction has been deliberate: required by decreasing input signal values. Large pixels (2 104
915 um²), thick sensors (maggiori di 200 um), and moderate sensor radiation damage for 1st generation
916 detectors translated into expected signals of order 10 ke, while small pixels (0.25 104 um²), thinner
917 sensors (100 um), and heavier sensor radiation damage will lead to signals as low as 2 ke at the
918 HL-LHC
919 The ENC can be directly calculated by the Cumulative Distribution Function (CDF) (scurve)
920 obtained from the discriminator "hit" pulse response to multiple charge injections
921 Radiation damages oxide layer causes shift of MOSFET threshold voltage

923 **6.2 TJ-Monopix1 characterization**

924 **6.2.1 Threshold and noise dispersion**

925 Un plot con s curve e residui (perchè dovrebbe essere migliore il modello con doppia retta? sul
926 RD53 c'era scritto, trovalo e leggilo) Istogrammi e colormap
927

928 **6.2.2 Absolute calibration of ToT**

929 Misure con il ferro. Metti un plot di singolo pixel dello spettro del ferro fittato con CB. Perchè
930 CB? rimuovere i cluster comunque lasciava una coda abbastanza grande a sx e fittare con una
931 gaussiana comunque non dava risultati migliori.

932 **6.3 ARCADIA-MD1 characterization**

933 **Chapter 7**

934 **Test beam measurements**

935 **7.1 Testbeam motivation**

936 Possibilità di integrare carica sul pixel: due elettroni consecutivi su un pixel ogni quanto arrivano?

937 Vogliamo sfruttare l'analog pile up, per fare questo dobbiamo fare attenzione a non finire nel
938 digital pile up Devi avere che il tot dell'elettrone (cioè MIP) è maggiore del deltat medio; in questo
939 caso potresti riuscire ad integrare carica. Non è possibile rivelare singoli elettroni in quanto l'hit
940 rate è troppo alto per le dosi messe a disposizioni con il fascio. Una formula di conversione è:

$$R[Hz/cm^2] = \frac{DPP[Gy]}{1.6 \cdot 10^{10} S[g/cm^2]} \quad (7.1)$$

941 where S is the stopping power in water, $2.17 g/cm^2$ The medium is ordinarily water, since dosimetric
942 protocols are based on measurements in water as reference

943 La struttura del fascio e le varie quantità che si usano per descriverlo sono riportate in figure
944 7.1. Ricordo i valori tipici che stanno in tabella in table ??.

945 **7.2 Apparatus description**

946 **7.3 Measurements**

947 Numero di hit in funzione del DDP. Spettri con e senza collimatori.

Table 1. Terminology used throughout the text.

Term	Symbol	Description
intra-pulse dose-rate	—	The duration of a single pulse. ^a
	\bar{D}	Mean dose-rate for a multi-pulse delivery.
pulse repetition frequency	\dot{D}_p	Dose-rate in a single pulse. ^a
	DPP	Dose in a single pulse. ^a
	PRF	Number of pulses delivered per unit time. ^a
	t_i	Total irradiation time from the beginning of the first delivered pulse to the end of the last delivered pulse.
ultrahigh dose-rate	—	Radiation delivered with mean dose-rate of $> \sim 40 \text{ Gy s}^{-1}$.
	—	Ultrahigh dose-rate RT that presents decreased damage to normal tissues compared to RT delivered with conventional dose-rate of $\sim 0.04 \text{ Gy s}^{-1}$.

^aPulses are considered to be macro-pulses unless otherwise stated (see also figure 1).

^bIn literature sometimes referred to as the instantaneous dose-rate.

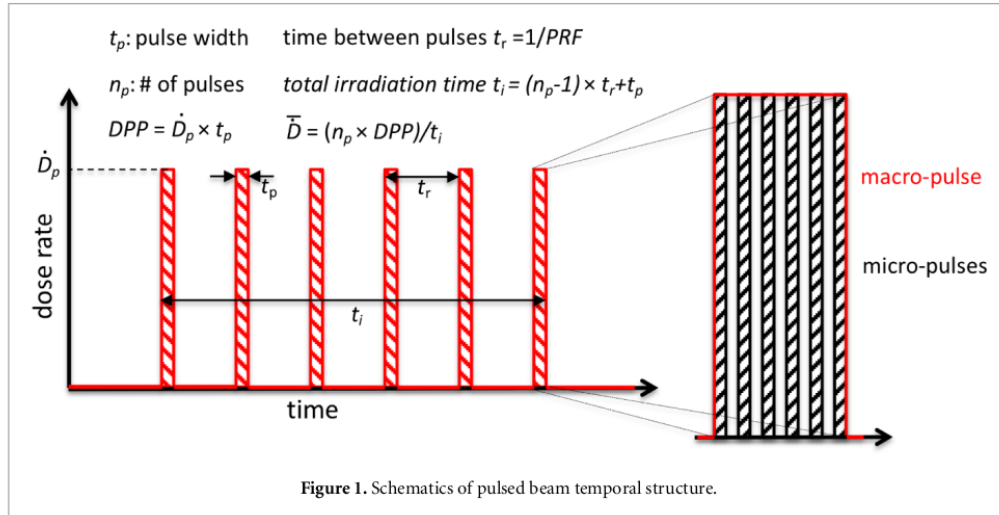


Figure 7.1

948 Appendix A

949 Pixels detector: a brief overview

950 A.1 Radiation damages

951 Radiation hardness is a fundamental requirement for pixels detector especially in HEP since they
 952 are almost always installed near the interaction point where there is a high energy level of radiation.
 953 At LHC the ϕ_{eq} per year in the innermost pixel detector is $10^{14} n_{eq}/cm^2$; this number reduces by
 954 an order passing to the outer tracker layer [2] pag 341 Wermes. Here the high fluence of particles
 955 can cause a damage both in the substrate of the detector and in the superficial electronics.

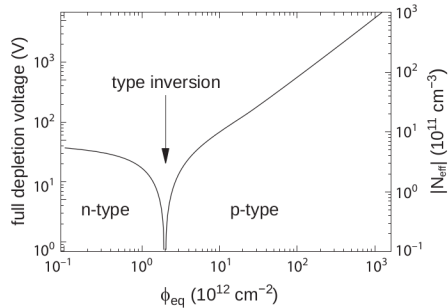
956 The first one has a principal non ionizing nature, due to a non ionizing energy loss (NIEL), but
 957 it is related with the dislocation of the lattice caused by the collision with nuclei; by this fact the
 958 NIEL hypothesis states that the substrate damage is normalized to the damage caused by 1 MeV
 959 neutrons. Differently, surface damages are principally due to ionizing energy loss.

960 **DUE PAROLE IN PIÙ SUL SURFACE DAMAGE** A charge accumulation in oxide (SiO_2) can
 961 cause the generation of parasitic current with an obvious increase of the 1/f noise. Surface damages
 962 are mostly less relevant than the previous one, since with the development of microelectronics and
 963 with the miniaturization of components (in electronic industry 6-7 nm transistors are already used,
 964 while for MAPS the dimensions of components is around 180 nm) the quantity of oxide in circuit
 965 is reduced.

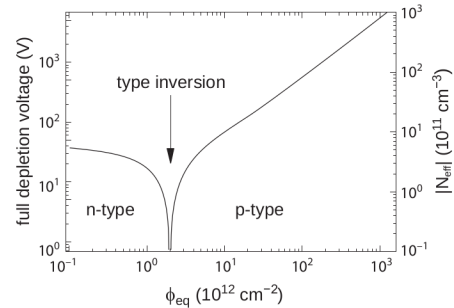
966 Let's spend instead two more other words on the more-relevant substrate damages: the general
 967 result of high radiation level is the creation of new energy levels within the silicon band gap and
 968 depending on their energy-location their effect can be different, as described in the Shockely-Read-
 969 Hall (SRH) statistical model. The three main consequence of radiation damages are the changing
 970 of the effect doping concentration, the leakage current and the increasing of trapping probability.

971 **Changing of the effective doping concentration:** is associated with the creation/removal
 972 of donors and acceptors center which trap respectively electrons/holes from the conduction band
 973 and cause a change in effective space charge density. Even an inversion (p-type becomes n-type¹)
 974 can happen: indeed it is quite common at not too high fluences ($\phi_{eq} 10^{12-13} n_{eq} cm^{-2}$). A changing
 975 in the doping concentration requires an adjustment of the biasing of the sensor during its lifetime
 976 (eq.2.1) and sometimes can be difficult keeping to fully deplete the bulk.

¹L'INVERSIONE OPPOSTA NON CE L'HA PERCHÈ?



(a) 1a



(b) 1b

977 **Leakage current:** is associated with the generation-recombination centers. It has a strong
978 dependence with the temperature ($I_{leak} \propto T^2$), whose solution is therefore to operate at lower
979 temperature.

980 **Increase of trapping probability:** since the trapping probability is constant in the depleted
981 region, the collected charge decreases exponentially with the drift path. The exponential coefficient,
982 that is the mean trapping path, decreases after irradiation and typical values are 125-250 μm and
983 must be compared with the thickness of the depleted region which () corresponds to the mean drift
984 path.

985 Different choices for substrate resistivity, for junctions type and for detector design are typically
986 made to fight radiation issues. Some material with high oxygen concentration (as crystal produced
987 using Czochralki (Cz) or float-zone (Fz) process (**CONTROLLA LA DIFFERENZA TRA I DUE**))
988 for example, show a compensation effect for radiation damage; another example is the usage of
989 n+ -in-p/n sensors (even if p+ -in-n sensors are easier and cheaper to obtain) to get advantage
990 of inversion/to have not the inversion (since they are already p-type). After inversion the n+p
991 boundary, coming from n+ in-n, but to keep using the sensor the depletion zone still must be
992 placed near the diode.

993 Single Event Upset, in sostanza è quando un bit ti cambia valore (da 0 a 1 o viceversa) perché
994 una particella deposita carica nell'elettronica che fa da memoria registro/RAM/.... Questo tipo
995 di elettronica ha bisogno di un sacco di carica prima che il bit si "flippi" (cambi valore), infatti
996 tipicamente per avere un SEU non basta una MIP che attraversa esattamente quel pezzo di chip
997 in cui è implementata la memoria, ma un adrone che faccia interazione nucleare producendo più
998 carica di quanto farebbe una MIP. Questo metodo pur essendo più comodo richiede less amount of
999 area ha però come drawback che il registro può essere soggetto a SEU problema non trascurabile
1000 in acceleratori come HL-LHC adronici

1001 Bibliography

- 1002 [1] W. Snoeys et al. “A process modification for CMOS monolithic active pixel sensors for
1003 enhanced depletion, timing performance and radiation tolerance”. In: (2017). DOI: <https://doi.org/10.1016/j.nima.2017.07.046>.
- 1005 [2] H. Kolanoski and N. Wermes. *Particle Detectors: Fundamentals and Applications*. OXFORD
1006 University Press, 2020. ISBN: 9780198520115.
- 1007 [3] E. Mandelli. “Digital Column Readout Architecture for 10.1109/NSSMIC.2009.5402399 the
1008 ATLAS Pixel 0.25 um Front End IC”. In: (2002).
- 1009 [4] M. Garcia-Sciveres and N. Wermes. “A review of advances in pixel detectors for experiments
1010 with high rate and radiation”. In: (2018). DOI: <https://doi.org/10.1088/1361-6633/aab064>.
- 1012 [5] C. Marinas. “The Belle-II DEPFET pixel detector: A step forward in vertexing in the su-
1013 perKEKB flavour factory”. In: (2011). DOI: [doi:10.1016/j.nima.2010.12.116](https://doi.org/10.1016/j.nima.2010.12.116).
- 1014 [6] J. Baudot. “First Test Results Of MIMOSA-26, A Fast CMOS Sensor With Integrated Zero
1015 Suppression And Digitized Output”. In: (2010). DOI: [doi:10.1109/NSSMIC.2009.5402399](https://doi.org/10.1109/NSSMIC.2009.5402399).
- 1016 [7] A. Dorokhov. “High resistivity CMOS pixel sensors and their application to the STAR PXL
1017 detector”. In: (2011). DOI: [doi:10.1016/j.nima.2010.12.112](https://doi.org/10.1016/j.nima.2010.12.112).
- 1018 [8] Giacomo Contin. “The STAR MAPS-based PiXeL detector”. In: (2018). DOI: <https://doi.org/10.1016/j.nima.2018.03.003>.
- 1019 [9] Nolan Espplen. “Physics and biology of ultrahigh dose-rate (FLASH) radiotherapy: a topical
1020 review”. In: (2020). DOI: <https://doi.org/10.1088/1361-6560/abaa28>.
- 1022 [10] M. Dyndal et al. “Mini-MALTA: Radiation hard pixel designs for small-electrode monolithic
1023 CMOS sensors for the High Luminosity LHC”. In: (2019). DOI: <https://doi.org/10.1088/1748-0221/15/02/p02005>.
- 1025 [11] M. Barbero. “Radiation hard DMAPS pixel sensors in 150 nm CMOS technology for opera-
1026 tion at LHC”. In: (2020). DOI: <https://doi.org/10.1088/1748-0221/15/05/p05013>.
- 1027 [12] K. Moustakas et al. “CMOS Monolithic Pixel Sensors based on the Column-Drain Architec-
1028 ture for the HL-LHC Upgrade”. In: (2018). DOI: <https://doi.org/10.1016/j.nima.2018.09.100>.
- 1030 [13] I. Caicedo et al. “The Monopix chips: depleted monolithic active pixel sensors with a column-
1031 drain read-out architecture for the ATLAS Inner Tracker upgrade”. In: (2019). DOI: <https://doi.org/10.1088/1748-0221/14/06/C06006>.
- 1033 [14] D. Kim et al. “Front end optimization for the monolithic active pixel sensor of the ALICE
1034 Inner Tracking System upgrade”. In: *JINST* (2016). DOI: [doi:10.1088/1748-0221/11/02/C02042](https://doi.org/10.1088/1748-0221/11/02/C02042).
- 1036 [15] L. Pancheri et al. “A 110 nm CMOS process for fully-depleted pixel sensors”. In: (2019). DOI:
1037 <https://doi.org/10.1088/1748-0221/14/06/c06016>.
- 1038 [16] L. Pancheri et al. “Fully Depleted MAPS in 110-nm CMOS Process With 100–300-um Active
1039 Substrate”. In: (2020). DOI: [10.1109/TED.2020.2985639](https://doi.org/10.1109/TED.2020.2985639).